This is a preprint, the final version is subject to change, of the American Mineralogist (MSA)
Cite as Authors (Year) Title. American Mineralogist, in press.
DOI: https://doi.org/10.2138/am-2020-7226

1 **Revision 1**

2 Zircon and Apatite Geochemical Constraints on the Formation of the Huojihe
3 Porphyry Mo Deposit in the Lesser Xing'an Range, NE China

4

5 Kai Xing[1, 2], Qihai Shu[1]*, David R. Lentz[2], Fangyue Wang[3]

6

7 [1] State Key Laboratory of Geological Processes and Mineral Resources, and School of
8 Earth Sciences and Resources, China University of Geosciences, Beijing 100083, China
9 [2] Department of Earth Sciences, University of New Brunswick, Fredericton, NB E3B
10 5A3, Canada
11 [3] Ore Deposit and Exploration Center (ODEC), Hefei University of Technology, Hefei
12 230009, Anhui, China

13

14 * Corresponding author: qshu@cugb.edu.cn (Qihai Shu)

15

This is a preprint, the final version is subject to change, of the American Mineralogist (MSA)
Cite as Authors (Year) Title. American Mineralogist, in press.
DOI: https://doi.org/10.2138/am-2020-7226

ABSTRACT

Northeastern China is an important Mo resource region in China, with more than 80 Mo deposits and occurrences. The Huojihe deposit located in the Lesser Xing'an Range represents one of the many Mesozoic porphyry Mo deposits in NE China, and has been selected for further investigation attempting to clarify the possible mechanisms controlling Mo mineralization. In this study, accessory minerals including zircon and apatite from the causative intrusions (biotite monzogranite and granodiorite) have been analyzed to reveal their chemical and isotopic compositions, which provide insights into the nature of the source magmas and a better understanding of the factors affecting their mineralization potential.

Zircon U-Pb dating shows that the biotite monzogranite from the Huojihe deposit formed at 181.6 ± 0.6 Ma, which is identical to the previously reported molybdenite Re-Os age (~181 Ma), indicating that the intrusion is probably genetically related to the Mo mineralization. The intrusion samples share homogeneous geochemical and Sr-Nd isotopic compositions, with initial $^{87}Sr/^{86}Sr$ ratios of 0.7072–0.7075 and slightly negative $\varepsilon_{Nd}(t)$ values from -2.3 to -1.4, reflecting a uniform magma source. The least-altered apatites show similar (or slightly enriched) initial $^{87}Sr/^{86}Sr$ ratios (0.7080–0.7108) and $\varepsilon_{Nd}(t)$ values (-4.0 to -1.8), whereas the hydrothermally altered apatites are characterized by significantly higher initial $^{87}Sr/^{86}Sr$ ratios (0.7091–0.7119) and more negative $\varepsilon_{Nd}(t)$ values (-4.9 to -4.4), probably due to the interaction between the hydrothermal fluids and wall rocks. The zircon $\varepsilon_{Hf}(t)$ values vary from -0.9 to 1.7, corresponding to a restricted range of T_{DM2} ages from 1279 to 1120 Ma. The Sr-Nd-Hf isotope results suggest that the primary magmas associated with the Mo mineralization could be generated from a

dominantly Mesoproterozoic lower crust source, with rare contribution from the depleted mantle. The low Ga and Ce and high Eu contents in the magmatic apatite demonstrate that the original magmas have a relatively high oxygen fugacity, which is also supported by the high zircon Ce_N/Ce_N^* (22–568) and Eu_N/Eu_N^* (0.38–0.71) values.

Estimates of absolute sulfur concentrations in the mineralization-related melt using available partitioning models for apatite return relatively low magmatic sulfur concentrations in Huojihe (20–100 ppm), indistinguishable from those of larger or smaller deposits or even barren magmatic bodies. Using the sulfur concentration data, a minimum volume of 10–50 km^3 magma has been suggested to be necessary to produce the Huojihe Mo deposit based on mass balance modelling. Besides, the Mo concentration in the original magma have also been roughly estimated based on the magma size (10–50 km^3) and the contained Mo in Huojihe (0.275 Mt). The magmatic Mo concentrations (2–10 ppm) are similar to many other porphyry Mo systems (e.g., the Climax-type porphyry Mo deposits), and are also comparable to subeconomic to barren magma systems. This study suggests that pre-degassing enrichments of Mo and S in the original magma is not necessarily important in the formation of the Huojihe Mo deposit; rather, factors other than melt composition may be more critical in forming a porphyry Mo deposit. This understanding might also apply to other porphyry Mo mineralized systems worldwide.

Keywords: Apatite and zircon geochemistry, magmatic S and Mo contents, mineralization mechanism, Huojihe porphyry Mo deposit, NE China

This is a preprint, the final version is subject to change, of the American Mineralogist (MSA)
Cite as Authors (Year) Title. American Mineralogist, in press.
DOI: https://doi.org/10.2138/am-2020-7226

61 ## INTRODUCTION

62 In the past decade, more than 80 porphyry Mo deposits have been discovered in NE
63 China, resulting in a total Mo metal resource of >11.4 Mt (Shu et al. 2016; Chen et al.
64 2017). These deposits are generally characterized by high abundances of Mo with little or
65 no Cu. Many of them have Jurassic to Early Cretaceous ages and have been suggested to
66 be related to magmatic events during the subduction or subsequent slab rollback of the
67 Paleo-Pacific oceanic plate (Wu et al. 2011; Ouyang et al. 2013; Shu et al. 2016; Zhai et
68 al. 2018). However, to date it is still unclear what factors have controlled the large-scale
69 Mesozoic porphyry Mo mineralization in this region. Whether there is any inherent Mo
70 enrichment of the source region and/or any pre-degassing magma processes leading to
71 high-Mo melts remains enigmatic. In recent years, melt inclusion compositional studies
72 of the Climax-type porphyry Mo deposits from North America have demonstrated that
73 the Mo-related magmas do not contain more Mo than any other magmas in subeconomic
74 or barren systems, and therefore a Mo-rich magma is not necessarily required to form an
75 economic Mo deposit (e.g., Audétat 2010, 2015; Lerchbaumer and Audétat 2013; Mercer
76 et al. 2015; Audétat and Li 2017; Zhang and Audétat 2017a, b). However, no melt
77 inclusion has been recognized in the porphyry Mo deposits in NE China, which hampers
78 the understanding of the Mo concentrations of the causative melts.

79 Zircon and apatite are common magmatic accessory minerals resistant to weathering
80 and weak hydrothermal alteration (Belousova et al. 2002a, b; Cook et al. 2016); therefore
81 magmatic zircon and apatite can preserve considerable physicochemical information of
82 their equilibrium magmas (e.g., Watson 1980; Ballard et al. 2002; Piccoli and Candela
83 2002; Mathez and Webster 2005; Dilles et al. 2015; Pan et al. 2016; Azadbakht et al.

2018). For example, zircon Hf and apatite Sr-Nd isotopic compositions have been widely used to trace magma source (e.g., Zhao et al. 2015; Zeng et al. 2016), Ce and Eu anomalies of zircon and apatite have been used to quantify magma oxidation state (e.g., Ballard et al. 2002; Cao et al. 2012; Chelle-Michou et al. 2014; Dilles et al. 2015; Lu et al. 2016; Pan et al. 2016; Shu et al. 2019), while halogens and sulfur contents of magmatic apatite are important indicators for evaluating magma fertility (e.g., Pan and Fleet 2002; Coulson et al. 2001; Chelle-Michou et al. 2017; Richards et al. 2017; Zhu et al. 2018).

The Huojihe Mo deposit is a typical porphyry deposit in the Lesser Xing'an Range, NE China, with 0.275 Mt Mo at an average grade of 0.07% (Tan et al. 2013). In this paper, systematic element and isotopic compositions have been analyzed in apatite and zircon from the granitic intrusions related to the Mo mineralization in Huojihe. Zircon Hf and apatite (and also whole rock) Sr-Nd isotopes were used to reveal the magma source regions, while the elemental compositions of both minerals have provided insights into the nature of the ore-forming magmas. The results from this study are helpful in understanding the possible factors controlling the Mo mineralization in Huojihe, and probably in other porphyry Mo deposits in NE China and worldwide.

GEOLOGICAL BACKGROUND

Northeastern China is located within the east portion of the Central Asian Orogen Belt, which lies between the Siberian and North China cratons (Sengör and Natal'in 1996; Wu et al. 2011). Northeastern China has undergone two major stages of evolution under different tectonic regimes. During the Paleozoic, amalgamation of several micro-continent blocks, including Erguna, Xing'an, Songliao, and Liaoyuan terranes

from north to south, occurred as a consequence of the subduction and closure of the Paleo-Asian ocean. Later in the Mesozoic, this region was dominated by the Paleo-Pacific subduction in the east, resulting in intense magmatism and metal mineralization (Fig. 1a; Wu et al. 2011; Ouyang et al. 2013; Shu et al. 2016; Chen et al. 2017; Deng et al. 2017).

The Lesser Xing'an Range lies in the north part of the Songliao terrane in NE China (Fig. 1a). Strata outcropping in this region include Paleozoic volcanic and metamorphic rocks (Yang et al. 2012; Zhang et al. 2017), Mesozoic volcanic rocks, and Quaternary sediments. The regional structures are characterized by faults striking NNW and NE, with the NE-striking Yitong-Yilan Fault crosscutting the NNW-striking Mudanjiang Fault (Fig. 1a, b). Phanerozoic granitic intrusions are widespread in the region (Fig. 1b). The Mesozoic granitoids cover most areas of the Lesser Xing'an Range, while Paleozoic intrusions are less abundant. Many porphyry, skarn, and epithermal deposits with Mesozoic ages in this area are genetically associated with these granitic intrusions (e.g., Hu et al. 2014, 2019; Deng and Wang 2016; Shu et al. 2016; Chen et al. 2017; Zhang et al. 2017; Chen and Zhang 2018; Fei et al. 2018).

The Huojihe porphyry Mo deposit is located in the north segment of the Lesser Xing'an Range, which occupies an area of ~9 km^2. The deposit is composed of two mineralization zones, including a dominant eastern section and a subordinate western section, which are separated by a NNW-trending fault (Fig. 2a). In the Huojihe mining area, in addition to the granitic intrusions, the intermediate-acidic volcanic rocks are the only exposed rocks belonging to the middle Permian Wudaoling Formation (Fig. 2a). The granitic intrusions are dominated by biotite monzogranite and granodiorite with minor

alkali-feldspar granite (Fig. 2a, b). The biotite monzogranite and granodiorite are the major host to the orebodies (Fig. 3). The biotite monzogranite is generally composed of quartz (~30%), plagioclase (~25%), K-feldspar (~30%), biotite (~13%), and accessory minerals including apatite, zircon, and titanite (~2%; Fig. 3b, c, d). The granodiorite is composed of quartz (~20%), plagioclase (~50%), K-feldspar (~15%), biotite (~10%), amphibole (~3%), and also minor accessory minerals (~2%, apatite, zircon, and titanite; Fig. 3a, e).

Hydrothermal alteration types are widely developed in the Huojihe deposit and commonly overlap. Several major alteration styles can be identified in the granitic intrusions, including potassic, phyllic, propylitic, and to a lesser extent, argillic alteration. The potassic alteration is pervasive and closely related to the Mo mineralization. It is represented by quartz-molybdenite veins with K-feldspar halos (Fig. 3c, e). The potassic alteration is commonly overprinted by later phyllic alteration. A total of 37 economic orebodies have been discovered in Huojihe, and most of the ores occur as veins, breccias, or disseminated in the intrusions. Ore minerals are dominated by molybdenite with some chalcopyrite and pyrite (Fig. 3).

SAMPLES AND METHODS

Samples

Samples of the granitic intrusions were collected from several typical drill cores of the prospecting line 7 (i.e., the A-A' line in Fig. 2). Three biotite monzogranite samples and one granodiorite sample were selected for apatite geochemical and Sr-Nd isotopic

analyses, one biotite monzogranite sample was selected for zircon U-Pb dating, Hf isotope, and trace element analyses, and four samples (including two biotite monzogranite and two granodiorite samples) were collected for whole rock compositional and Sr-Nd isotopic analyses.

Whole rock compositions and Sr-Nd isotopic analyses

The granitic samples used for whole rock compositional and Sr-Nd isotopic analyses were first washed and trimmed to remove weathered surfaces; the fresh portions were crushed and pulverized to 200 mesh. Whole rock major and trace elements were measured at the Geochemistry Lab in China University of Geosciences, Beijing. Contents of major elemental oxides were analyzed using a Leeman Prodigy inductively coupled plasma-optical emission spectroscopy (ICP-OES) of a fused bead dissolved in nitric acid, and the analytical precisions for most major elements were better than 1% after repeated measurements of rock reference standards GSR-1, GSR-3 (National Geological Standard Reference Materials of China), and AGV-2 (US Geological Survey). Loss on ignition (LOI) was determined after heating the samples at 1000 °C for several hours before being cooled in a desiccator and reweighed. Trace elements were measured by an Agilent-7500a inductively coupled plasma-mass spectrometry (ICP-MS) of a fused bead digested in nitric acid, yielding an analytical uncertainty of <5% for most of the elements. The standards GSR-1and AGV-2 were also used to monitor the analytical accuracy.

For whole rock Sr-Nd isotopes, 150–200 mg of the rock powders were dissolved in a mixture of HNO_3 + HF under 80 °C for seven days. Rb, Sr, Sm, and Nd were separated and purified via a second cation-exchange column at the Key Laboratory of Orogenic Belts and Crustal Evolution, Peking University. Sr-Nd isotopic analyses were carried out

using a Thermo-Finnigan TRITON thermal ionization mass spectrometer (TIMS) by the isotope dilution method at the Tianjin Institute of Geology and Mineral Resources, China Geological Survey, following the analytical procedures described by Liu et al. (2017). Standards NBS-987 and LRIG were used as the reference materials for Sr and Nd, respectively, whereas the reference material BCR-2 (Columbia River Basalt 2) was used to monitor the analytical accuracy. The mass fractionation was corrected by normalizing the measured $^{87}Sr/^{86}Sr$ and $^{143}Nd/^{144}Nd$ ratios against $^{86}Sr/^{88}Sr$ ratio of 0.1194 and $^{146}Nd/^{144}Nd$ ratio of 0.7219, respectively. The analytical errors were <1% for Rb and Sr, and <0.5% for Sm and Nd. The decay constant of ^{87}Rb used to calculated the initial Sr isotopic ratios is 1.42×10^{-11} $year^{-1}$, and that of ^{147}Sm used to calculated the model ages and $\varepsilon_{Nd}(t)$ is 6.54×10^{-12} $year^{-1}$. All the data reduction was performed using the method described in Jahn et al. (1996), while the two-stage Nd model ages were calculated following the same assumption by Keto and Jacobsen (1987).

Apatite and biotite geochemical analyses

Optical microscopic cathodoluminescence (OP-CL) images of apatite were taken on polished thick sections using a Cambridge Image Technology cold CL unit model Mk5 mounted on a petrographic microscope at the Faculty of Earth Resources, China University of Geosciences, Wuhan. Apatite and biotite major element compositions were determined by electron microprobe using a JXA-8230 superprobe equipped with wavelength-dispersive spectrometers at the Center of Material Research and Analysis, Wuhan University of Technology, China. The minerals were analyzed under an accelerating voltage of 15 kV and a probe current of 20 nA. The beam spot diameter was 5 μm and the average detection limits for each element were 0.01%. The analyzed

198 elements include F, Na, Mg, Al, Si, P, S, Cl, Ca, Ti, Mn, and Fe. In order to minimize the
199 effects of EPMA-operating conditions on the halogen intensities, the apatite grains
200 oriented with the c-axis parallel to the incident electron beam were preferentially selected
201 for analysis (e.g., Stormer et al.1993; Pyle et al. 2002; Goldoff et al. 2012; Stock et al.
202 2015), and F, Cl and Ca were measured first with shorter counting times of 10 s for peak
203 after 5 s for background, whereas the rest more stable elements were analyzed
204 subsequently with longer counting times on a peak/background of 30/15 s. The standards
205 include fluorite for F, albite for Na, chrome-diopside for Mg, garnet for Al, almandine for
206 Si, fluorapatite for P and Ca, barite for S, tugtupite for Cl, rutile for Ti, rhodonite for Mn
207 and hematite for Fe. The chemical formula for apatite was calculated following the
208 method proposed by Ketcham (2015).

209 Trace elements in apatite were measured by laser ablation-inductively coupled
210 plasma-mass spectrometry (LA-ICP-MS) on polished sections at the Ore Deposit and
211 Exploration Centre, Hefei University of Technology. The analyses were carried out on an
212 Agilent 7900 ICP-MS instrument, which was coupled to a Cetac Analyte HE
213 laser-ablation system. Each analysis was performed by a uniform spot size diameter of 30
214 μm at 7 Hz with an energy of ~4 J/cm^2 for ~40 s after measuring the gas blank for ~20 s.
215 Argon was used as the make-up gas and mixed with the carrier gas He via a T-connector
216 before entering the ICP (Wang et al. 2017). Ca was used as the internal standard, whereas
217 external standard materials include NIST 610, NIST 612, and BCR 2G, which were run
218 after each 10 unknowns. The detection limits were calculated for each element in each
219 spot analysis. The off-line data processing was performed using the program
220 ICPMSDataCal (Liu et al. 2008). The analytical uncertainties were generally lower than

221 10% for most of the trace elements.

222 **Apatite Sr-Nd isotope analyses**

223 *In situ* Sr and Nd isotopic analyses of apatite were carried out using
224 multiple-collector-inductively coupled plasma-mass spectrometry (MC-ICP-MS; Neptune
225 Plus) connected with a Newwave 213-nm laser ablation system. Helium was used as the
226 carrier gas to transport the ablated materials, which was then mixed with purified argon
227 and nitrogen before entering the ICP torch. Data acquisition was composed of ~20 s
228 ablation for Sr and ~30 s for Nd, both after ~10 s background measurement, using spot
229 sizes of 80 μm at a repetition pulse rate of 10 Hz and energy density of 15 J/cm^2. All the
230 Sr and Nd isotopic compositions were calibrated against the reference material Durango
231 (Foster and Vance 2006). The analytical uncertainties were <0.015% for $^{87}Sr/^{86}Sr$ and
232 <0.005% for $^{143}Nd/^{144}Nd$. Apatite Sr-Nd isotopic data reduction was performed using the
233 same methods for the whole rock samples mentioned above.

234 **Zircon U-Pb dating, trace element, and Hf isotope analyses**

235 Single zircon grains analyzed in this study were separated from rock samples using
236 heavy liquid and magnetic methods, followed by handpicking under a binocular
237 microscope. Zircon grains were mounted in an epoxy block, polished, and examined
238 using cathodoluminescence (CL) images to choose suitable targets for *in situ* elemental
239 and isotopic analyses.

240 Zircon U-Pb dating and trace element analyses were conducted synchronously using
241 LA-ICP-MS in the Institute of Geology, Chinese Academy of Geological Sciences,
242 Beijing. An Agilent 7900 ICP-MS coupled with an NWR 193^{UC} laser ablation system was

used, and the analyses were performed using 30 μm diameter spot at 5 Hz repetition rate and 2.3 J/cm^2 laser fluence. The zircon 91500 and NIST610 standards were used as the primary reference materials, while the GJ-1 and Plešovice were used for data quality assessment. The data reduction was conducted using the Iolite software package (Paton et al. 2010) and the weighted mean $^{206}Pb/^{238}U$ age was calculated using the Isoplot 3.0 program (Ludwig 2003).

In situ zircon Hf isotopic analysis was subsequently determined using a MC-ICP-MS (Thermo Fisher Neptune Plus) equipped with a femtosecond ASI J200 laser ablation system at the National Research Center of Geoanalysis in Beijing. The laser fluence on the sample surface was ~7 J/cm^2, the repetition rate was 10 Hz, and the resulting craters were approximately 40 × 20 μm. The Plešovice zircon standard was used for data calibration with recommended $^{176}Hf/^{177}Hf$ ratios of 0.282482. The isobaric interference of ^{176}Yb and ^{176}Lu on ^{176}Hf was corrected following Fisher et al. (2014). The decay constant for ^{176}Lu (1.865×10^{-11} year^{-1}) proposed by Scherer et al. (2001) and the present-day chondritic ratios ($^{176}Hf/^{177}Hf$ = 0.282772 and $^{176}Lu/^{177}Hf$ = 0.0332) from Blichert-Toft and Albarède (1997) were adopted to calculate the $\varepsilon_{Hf}(t)$ values. The single-stage model ages (T_{DM1}) were calculated relative to the depleted mantle with a present day $^{176}Hf/^{177}Hf$ ratio of 0.28325 and $^{176}Lu/^{177}Hf$ of 0.0384 (Vervoort and Blichert-Toft 1999), while the two-stage Hf model ages (T_{DM2}) were calculated on the assumption that the parent magma was produced from average continental crust with $^{176}Lu/^{177}Hf = 0.015$ (Griffin et al. 2000).

RESULTS

Whole rock Analysis

Whole rock geochemistry. Whole rock geochemical compositions for the granitic samples from the Huojihe deposit are listed in Appendix 1. These intrusions have relatively homogeneous major element compositions, including SiO_2 (66.86 to 68.61 wt %; n = 4), P_2O_5 (0.09 to 0.13 wt %), Al_2O_3 (15.14 to 15.42 wt %), and $Na_2O + K_2O$ (7.07 to 7.75 wt %). All the samples show typical enrichment of light rare earth elements (LREEs) and depletion of heavy rare earth elements (HREEs) (Appendix 2). They are moderately fractionated, yielding LREE/HREE ratios of 10.97–14.02 and $(La/Yb)_N$ ratios of 12.32–18.78 (Appendix 1).

Whole rock Sr-Nd isotopes. Whole rock Sr-Nd isotopic compositions of the intrusive rocks are presented in Appendix 3 and plotted in Fig. 4. The initial Sr isotopic ratios $(^{87}Sr/^{86}Sr)_i$ and $\varepsilon_{Nd}(t)$ values have been calculated on the basis of the obtained zircon U-Pb ages (181.6 Ma; details shown below) of the biotite monzogranite from this study. The uniform initial Sr isotope ratios range from 0.7072 to 0.7075 and the $\varepsilon_{Nd}(t)$ values range from -2.3 to -1.4, corresponding to two-stage Nd model ages of 1151–1081 Ma.

Apatite

Apatite petrography. Previous studies have documented that magmatic apatites can be partially or completely altered by hydrothermal fluids, which is a common process during the porphyry-type mineralization (e.g., Harlov and Förster 2003; Harlov 2015; Bouzari et al. 2016). In this study, careful petrographic observation has revealed two types of apatite in the Huojihe deposit: unaltered magmatic apatite (Ap_m) and hydrothermally altered apatite (Ap_h).

Ap_m is common in the Huojihe granitic samples as an accessory mineral, which often occurs as inclusions in biotite and to a lesser extent, in plagioclase (Fig. 5a-e), or else, as microphenocrysts in the groundmass. It is euhedral to subhedral, inclusion-free and transparent, with sizes ranging mainly from 50 to 350 μm. It is bright and homogeneous under back-scattered electron (BSE) imaging and often shows obvious oscillatory and/or core-rim textures (Fig. 5g, h). In OP-CL images, it often displays a homogeneous yellow-green luminescence (Fig. 5e, f).

Ap_h often partly or even completely replaces the magmatic apatite (Fig. 5b-e, h, i). The Ap_h grains commonly have irregular crystal shapes and inhomogeneous patches (Fig. 5b, c). Under BSE imaging, they exhibit apparently darker color than the unaltered magmatic cores (Fig. 5h), and pitted surfaces with visible voids and mineral inclusions, including monazite (Fig. 5i). In addition, they often show a typical unbalanced bright yellow-white luminescence (Fig. 5e).

Apatite major and trace element compositions. The compositions of the analyzed apatite, including both magmatic and altered grains, are listed in Appendix 4. Generally, the Ap_m grains have 41.22–43.35 wt % P_2O_5, 53.96–56.28 wt % CaO, 0–0.05 wt % MgO and 0–0.39 wt % FeO. The Na_2O, Al_2O_3, and TiO_2 contents are mostly close to or below the detection limits, and when detected are 0–0.34 wt %, 0–0.03 wt %, and 0–0.18 wt %, respectively. The Ap_h has lower MnO concentrations (average 0.15 wt % MnO or 0.020 apfu Mn, where apfu refers to atoms per formula unit) than Ap_m (0.28 wt % MnO or 0.039 apfu Mn; Fig. 6a, e). Compared with the Ap_m (0.01–0.12 wt % or 0.003–0.035 apfu Cl). Ap_h also contains lower Cl (0.01–0.06 wt % or 0.002–0.016 apfu Cl; Fig. 6b). The SO_3 concentrations in Ap_m vary from 0.01 to 0.61 wt %, which vary from 0.04 to 0.50

311 wt % in Ap_h. The Ap_h has lower average concentrations of Y (344 ppm on average), Ce
312 (1160 ppm), and Nd (371 ppm) than the Ap_m (552 ppm Y, 1385 ppm Ce, and 525 ppm Nd;
313 Fig. 6c, d). The total REE concentrations (2734 ppm on average) of the Ap_h are also
314 lower than that of the Ap_m (3413 ppm on average). The calculated Eu anomaly ($\delta Eu = Eu_N/sqrt(Sm_N \times Gd_N)$, where "$_N$" indicates chondrite-normalized values) and Ce anomaly
316 ($\delta Ce = Ce_N/sqrt(La_N \times Pr_N)$) of Ap_m range from 0.14 to 1.50 and 0.89 to 1.11, respectively.
317 The X_F/X_{OH} and X_F/X_{Cl} ratios (X_F, X_{Cl}, and X_{OH} are the mole fractions of F, Cl, and OH,
318 respectively) of Ap_m are 3.44–94.78 and 48.62–587.0, respectively.

319 **Apatite Sr-Nd isotopes.** The Sr and Nd isotopic compositions of apatite are listed in
320 Appendix 4 and plotted in Fig. 4. The Ap_m ($^{87}Sr/^{86}Sr)_i$ values (calculated using the zircon
321 U-Pb age 181.6 Ma) range from 0.7080 to 0.7108, whereas the Ap_h ($^{87}Sr/^{86}Sr)_i$ values are
322 slightly higher, ranging from 0.7091 to 0.7119. The $^{147}Sm/^{144}Nd$ and $^{143}Nd/^{144}Nd$ ratios of
323 Ap_m are 0.0846–0.1885 and 0.51235–0.51244, respectively, whereas for the Ap_h, the
324 ratios are 0.0756–0.1571 and 0.51226–0.51234, respectively. Ap_h has slightly more
325 negative $\varepsilon_{Nd}(t)$ values ranging from -4.9 to -4.4 than the Ap_m (-4.0 to -1.8); the latter has a
326 two-stage Nd model age range between 1283 and 1110 Ma.

327 **Zircon**

328 **Zircon U-Pb ages.** Typical CL images of the zircon grains are shown in Fig. 7 and the
329 U-Pb dating results are summarized in Appendix 5. Zircon crystals from the biotite
330 monzogranite are euhedral and display typical magmatic oscillatory zoning under CL
331 imaging (Fig. 7b), with U/Th ratios varying from 1.0 to 2.9 (Appendix 5). All these
332 features suggest that these zircons have a magmatic origin and the U-Pb ages can
333 therefore represent the timing of magma emplacement. The weighted mean $^{206}Pb/^{238}U$

age is 181.6 ± 0.6 Ma (MSWD = 2.0, n = 31, Fig. 7a), which is interpreted to be the crystallization age of the biotite monzogranite.

Zircon trace elements. Zircon trace element compositions are listed in Appendix 5. The Ce and Eu contents are 9.40–69.90 ppm and 0.28–30.13 ppm, respectively. The zircon Eu anomaly ($Eu_N/Eu_N^* = Eu_N/sqrt(Sm_N \times Gd_N)$) range from 0.38 to 0.71 (Fig. 8c). The zircon Ce anomaly (Ce_N/Ce_N^*) is difficult to calculate reliably given the fact that the La and Pr contents in zircons from the Huojihe biotite monzogranite are extremely low and some are even below the detection limits (Appendix 5). We alternatively calculate the Ce anomaly following the proposed equation $Ce_N^* = Nd_N^2/Sm_N$ by Loader et al. (2017). Here the obtained zircon Ce_N/Ce_N^* ratios range from 22 to 568. In addition, the zircon Mo concentrations have also been obtained during analysis, varying from 0.15 to 0.33 ppm (Fig. 9).

Zircon Hf isotopes. The zircon grains for U-Pb dating were subsequently used for Hf isotopic analyses. Zircon Hf isotope results are listed in Appendix 5 and illustrated in Fig. 10. These zircons yield $^{176}Hf/^{177}Hf$ ratios from 0.282639 to 0.282708 and calculated $\varepsilon_{Hf}(t)$ values from -0.9 to 1.7 (Fig. 10), corresponding to T_{DM2} ages ranging between 1279 and 1120 Ma, in good agreement with the above whole-rock and apatite two-stage Nd model ages.

Biotite

Igneous biotite phenocrysts, which host apatite inclusions, were analyzed in this study. The measured biotite compositions were used to estimate biotite crystallization temperatures following the method of Henry et al. (2005) and the results can be found in Appendix 6. The Mg mole fractions (X_{Mg} = molar Mg/(Mg + Fe)) of the biotite vary

357 between 0.61 and 0.77, while the numbers of atoms per formula unit of Ti calculated on
358 the basis of 22 O atoms vary between 0.24 and 0.40 apfu (Appendix 6).

359

360 # DISCUSSION

361 ## Hydrothermal alteration

362 Apatite is relatively stable over a wide variety of geological processes including
363 weathering, transport, and weak hydrothermal alteration (Cook et al. 2016). However, it
364 has also been noted that acids can very likely alter the magmatic apatite and as a result,
365 the compositions would be partly or completely changed. Such a process is especially
366 common during the formation of intrusion-related hydrothermal deposits, including
367 predominantly porphyry, skarn, and high-sulfidation epithermal deposits (e.g., Harlov and
368 Förster 2003; Harlov 2015; Li and Zhou 2015; Bouzari et al. 2016). Therefore, only these
369 magmatic apatites without hydrothermal alteration can preserve the original
370 physiochemical information of the causative magma, whereas apatites, which have
371 experienced significant hydrothermal alteration, might offer insight into the intensity of
372 chemical exchanges during alteration (e.g., Bouzari et al. 2016).

373 In this study, Ap_h shows obvious depletion in Mn, Cl, Y, Ce, Nd, and REEs contents
374 (Fig. 6) compared with the Ap_m. The different geochemical compositions of the Ap_m and
375 Ap_h grains confirm that the Huojihe intrusions have undergone extensive metasomatism,
376 during which some of the magmatic apatites have been hydrothermally altered. The Ap_h
377 crystals have preserved the primary shape and orientation (Fig. 5b, h) of the original Ap_m,
378 but display sharp compositional boundaries with the Ap_m domains (Fig. 5b, d, e). They

379 also have pervasive micro-porosities and fluid inclusions (Fig. 5b, i). Such features are
380 consistent with a fluid-aided, coupled dissolution-reprecipitation process (Harlov et al.
381 2005; Li and Zhou 2015; Zeng et al. 2016). During dissolution-reprecipitation, elements
382 can be transported from the dissolving reaction front (original phase) to the
383 reprecipitating reaction front (new phase) via fluids, and a series of complex chemical
384 exchanges between apatite and the reactive fluid (Putnis 2009). As a result, many of the
385 trace elements, including Mn, Cl, Ce, Nd, Y, and REEs, have been leached out of the
386 reacted apatite and show a pronounced depletion (Fig. 6). This is consistent with the
387 experimental results and also similar to the element behavior observed in other minerals
388 during hydrothermal alteration (e.g., Harlov and Förster 2003; Harlov et al. 2005). In
389 addition, monazite inclusions can form in Ap_h (Fig. 5i) when the REEs are released
390 during fluid-aided alteration immediately reprecipitating into the new phases.

391 **Timing and petrogenesis of the Huojihe intrusions**

392 **Timing of magmatism.** Zircon U-Pb dating of the biotite monzogranite in the Huojihe
393 deposit indicates that it was emplaced at 181.6 ± 0.6 Ma. The U-Pb age is identical,
394 within error, to the U-Pb age of the granodiorite in Huojihe (182.1 ± 2.2 Ma; Sun et al.
395 2012), and is also consistent with previously reported molybdenite Re-Os ages 181.2 ±
396 1.8 Ma (Tan et al. 2013) and 180.7 ± 2.5 Ma (Zhang et al. 2014). Given that both the
397 monzogranite and granodiorite are potassically altered, are the major host to the
398 orebodies and that their emplacement is contemporaneous to the molybdenite
399 precipitation, it can be reasonably proposed that both the monzogranite and granodiorite
400 are the causative intrusions responsible for Mo mineralization. The early Jurassic age of
401 the Huojihe porphyry Mo deposit is also consistent with the regional magmatism and

mineralization, which have been widely accepted as a consequence of the flat-slab subduction of the Paleo-Pacific plate (Wu et al. 2011; Shu et al. 2016).

Petrogenesis of the causative intrusions. The biotite monzogranite and granodiorite share similar geochemical and isotopic compositions, suggesting that they are cogenetic. All samples have arc affinity with enrichment in large ion lithophile elements (LILEs), including Rb, Ba, Th, U, Pb, and Sr, and depletions in high field strength elements (HFSEs) including Nb, Ta, Zr, Ti, and P (Appendix 2). All the analyzed granitic samples are metaluminous, high-K calc-alkaline, with uniform A/CNK ratios (0.99–1.01), and can be classified as I-type (Appendix 7).

The apatite grains from the Huojihe intrusions have slightly higher $(^{87}Sr/^{86}Sr)_i$ and more negative $\varepsilon_{Nd}(t)$ values than the whole rock samples (Fig. 4), and this is the particular case for the hydrothermally altered Ap_h. This indicates that the Sr-Nd isotopic compositions of the apatite (especially the Ap_h) could have been slightly or significantly changed by the interaction between the ore-forming fluids and wall rocks during hydrothermal alteration (Zeng et al. 2016). The Ap_m grains and the whole rock samples should have similar Sr-Nd isotopic compositions, but the results from this study indicate that they are slightly different. This could be explained by the fact that most of the magmatic apatite grains have unaltered cores (often smaller than the laser diameter 80 μm) and altered rims (Fig. 5b, e, h), and the altered rims were probably partly ablated during the Sr-Nd isotopic analysis for the Ap_m domains, resulting in slightly higher $(^{87}Sr/^{86}Sr)_i$ ratios and more negative $\varepsilon_{Nd}(t)$ values for the Ap_m. The Sr-Nd isotopes in Huojihe are similar to many other late Triassic to early Jurassic magmatic-hydrothermal

mineralization systems in the Lesser Xing'an Range region (e.g., Luming, Xulaojiugou, and Cuihongshan; Fig. 4), together indicating a comparable magma source.

The zircon $\varepsilon_{Hf}(t)$ values (-0.9 to 1.7) of the Huojihe biotite monzogranite almost all fall within the field between the chondrite uniform reservoir and depleted mantle, with a uniform T_{DM2} age range of 1279–1120 Ma (Fig. 10). The basement in the Lesser Xing'an Range is mainly composed of the Dongfengshan Group, which has detrital zircons of various ages from ~2500 to ~750 Ma, with several peaks at 2.5–2.4 Ga, 1.8 Ga, 1.6–1.3 Ga, and ~820 Ma (e.g., Wu et al. 2000; Wang et al. 2014). The 1.6–1.3 Ga peak is consistent with the Nd and Hf model ages in this study, suggesting that the Huojihe granitoids were likely originated dominantly from the Mesoproterozoic lower crust, which could have mixed with minor depleted mantle materials. The zircon Hf isotopic compositions in Huojihe are also similar to several other granitic intrusions related to porphyry/skarn Mo deposits (Luming, Xulaojiugou, Cuihongshan, and Gaogangshan) in this region (Fig. 1b), all demonstrating a dominantly crustal source (Fig. 10). In contrast, the Au deposits including Tuanjiegou, Jinchang, and Dahuangling (all being early Cretaceous) in this region (Fig. 1b) have significantly higher zircon $\varepsilon_{Hf}(t)$ values for their syn-mineralization intrusions, indicative of more involvement of mantle materials (Fig. 10). The above difference can be explained by regional tectonic evolution. In the early Cretaceous, the northeastern China continent transitioned to an extensional setting due to the rollback of the subducted Paleo-Pacific plate, in which case asthenosphere upwelling would result in greater contributions from the mantle materials to magma generation (Zhang et al. 2010; Wu et al. 2011; Shu et al. 2016). Previous studies have documented that porphyry and epithermal Au deposits are commonly related to arc magmas that are

447 predominantly formed by partial melting of the metasomatized wedge of asthenospheric
448 mantle (e.g., Sillitoe and Hedenquist 2003; Richards 2009), whereas porphyry Mo
449 deposits are associated with magmas melted from older crust materials (e.g., Farmer and
450 DePaolo 1984; Klemm et al. 2008). This has also been confirmed in this study, with the
451 Mo-related intrusions having more enriched Hf isotopic compositions than the
452 Au-related intrusions (Fig. 10).

453 **The roles of the magma in the formation of the Huojihe porphyry Mo deposit**

454 Magmatic apatite can form at different stages of magma evolution and only those
455 crystallizing from a volatile-undersaturated melt can document the initial chemical
456 compositions of the melt responsible for the mineralization. This is because the contents
457 of various elements (especially volatiles) in the silicate melt would dramatically change
458 under volatile-saturated conditions as a function of the fluid/melt partition coefficient,
459 crystallization pressure, and water solubility (e.g., Audétat 2019). Therefore, apatite
460 crystals that equilibrate with a volatile-saturated melt would be likely depleted in many
461 elements (e.g., S), which couldn't record and preserve information of the parental
462 magmas (e.g., Stock et al. 2018; Audétat 2019).

463 Three magmatic apatite populations have been analyzed in the Huojihe deposit,
464 including biotite-hosted inclusions, plagioclase-hosted inclusions, and microphenocrysts
465 distributed in the groundmass. The F contents of most of these plagioclase-hosted apatite
466 inclusions (3.91 wt % on average) and apatite microphenocrysts (4.11 wt % on average)
467 are extremely high and exceed the maximum stoichiometric limit of 3.76 wt % (Pyle et al.
468 2002). They probably reflect either analytical errors, which could be induced by the
469 EPMA-operating conditions (e.g., Stormer et al. 1993; Goldoff et al. 2012), or residual F

enrichment, which are favored by melt during or after fluid exsolution under volatile-saturated conditions (e.g., Candela 1986). For the biotite-hosted apatite inclusions, they generally have higher Cl contents but lower F contents (Appendix 4). The host biotite near each of the apatite inclusions has been analyzed by electron microprobe to determine the compositions of different parts of the igneous biotite crystals (n = 8; Appendices 6 and 8). These would further be used to estimate the precipitation temperatures (approximately representing the crystallization temperatures of the neighboring apatite inclusions) following the empirical X_{Mg}-Ti-in-biotite geothermometry of Henry et al. (2005). The temperatures of one biotite crystal commonly decrease from core to rim, representing a gradually cooling process during its crystallization. Correspondingly, the inclusive apatite grains from the core to rim of most of the biotite crystals show typically decreasing trends for both the X_F/X_{OH} and X_F/X_{Cl} ratios (Appendix 8), which is indicative of a crystallization process under volatile-undersaturated conditions, as has been revealed by thermodynamic modelling (Stock et al. 2018). Therefore, most of the biotite-hosted apatite grains have preserved a record of the physicochemical features of the initial mineralization-related magmas before fluid exsolution in Huojihe. In the following discussion, only these Ap_m grains crystallized under volatile-undersaturated conditions (i.e., hosted in biotite) have been used.

Magma oxidation state. The abundances of Ce, Eu, and Ga in apatite can be used as proxies for the magmatic oxidation state (e.g., Streck and Dilles 1998; Sha and Chappell 1999; Prowatke and Klemme 2006; Cao et al. 2012; Chen and Zhang 2018). Eu, Ce, and Ga all have two ionic valences: Eu^{3+}/Eu^{2+}, Ce^{4+}/Ce^{3+}, and Ga^{3+}/Ga^{2+}, respectively. Eu^{3+},

493 Ce^{3+}, and Ga^{2+} are favored by apatite because they have a more comparable ionic radius
494 to Ca^{2+} and can therefore more preferentially substitute for Ca^{2+} in apatite (Sha and
495 Chappell 1999; Belousova et al. 2002b). As a result, apatite crystallized from oxidized
496 magmas will have higher Eu, but a lower amount of Ce and Ga (e.g., Cao et al. 2012;
497 Chen and Zhang 2018). As shown in Fig. 8a, the δEu and δCe of the Ap_m from the
498 Huojihe deposit are negatively correlated, confirming that they are likely controlled by
499 the oxidation state of the magma. A comparison of the magmatic apatite δEu, δCe, and
500 Ga contents from this study, with those reported from several other porphyry deposits and
501 barren igneous rocks, reveals that the Ap_m from the Huojihe porphyry Mo deposit have
502 relatively positive Eu and negative Ce anomalies. This suggests that the ore-related
503 magma in Huojihe could be relatively oxidized (Fig. 8a; Appendix 9). The result is also
504 supported by the Ga concentrations in the Ap_m, which are generally very low, i.e., lower
505 than many other porphyry deposits or barren igneous rocks (Fig. 8b).

506 Zircon Ce and Eu anomalies are also effective indicators of magmatic oxygen
507 fugacity (Dilles et al. 2015; Shen et al. 2015; Lu et al. 2016; Shu et al. 2019). In this study,
508 the calculated zircon Ce_N/Ce_N^* and Eu_N/Eu_N^* ratios vary from 22 to 568 and 0.38 to 0.71,
509 respectively (Fig. 8c). They overlap with the compiled results from other porphyry Mo or
510 Cu deposits, but are slightly higher than these from barren igneous rocks (Fig. 8c;
511 Appendix 9). The Ce and Eu anomalies of zircon agree well with that of apatite, together
512 demonstrating a relatively high magmatic oxygen fugacity in Huojihe, which has been
513 widely accepted as a prerequisite for porphyry-style Cu-Mo mineralization (e.g., Ballard
514 et al. 2002; Shen et al. 2015; Shu et al. 2019).

515 **Magma S content.** It has been traditionally proposed that high S concentrations in

516 oxidized magmas are important for the formation of a porphyry Cu (-Mo) deposit (e.g.,
517 Burnham 1979; Richards et al. 2017). The S concentrations in magmas can either be
518 directly measured from melt inclusions (e.g., Audétat 2015; Zhang and Audétat 2017a, b,
519 2018) or indirectly estimated using the S concentration values of S-rich minerals (e.g.,
520 apatite) taking into account the partitioning coefficients between melts and the
521 crystallized S-rich minerals (e.g., Chelle-Michou and Chiaradia 2017; Richards et al.
522 2017; Zhu et al. 2018). In Huojihe, the absence of melt inclusions in the magmatic
523 minerals precludes the possibility of directly obtaining the S contents of the original
524 magmas. Alternatively, the magma S contents have been calculated from the SO_3
525 concentrations of the Ap_m (i.e., 0.01–0.61 wt %; Appendix 10) using the two
526 recommended partition coefficient values for S between apatite and silicate melt from
527 Peng et al. (1997) and Parat et al. (2011). Although it has been suggested that S oxidation
528 states (S^{2-} and S^{4+}) other than S^{6+} may also substitute into the apatite structure, the high
529 magmatic oxygen fugacity in Huojihe indicates that the apatite S is dominated by S^{6+}
530 (Konecke et al. 2017). Using the equation of Parat et al. (2011), the magma S
531 concentrations have been estimated to be between 8 and 39 ppm (except for five
532 outliers >65 ppm; Appendix 10), with a median of 20 ppm. Using the method by Peng et
533 al. (1997), the calculated magma S concentrations range from 37 to 290 ppm (except for
534 two outliers, 6 ppm and 475 ppm; Appendix 10), with a median of 100 ppm. The above
535 results using the two methods differ from each other significantly, as has also been noted
536 by Chelle-Michou and Chiaradia (2017). Nevertheless, it can still be reasonably
537 concluded that the pre-degassing S concentrations in the Huojihe magma are 20–100 ppm.
538 The results are comparable with the estimated S concentrations using apatite SO_3

539 concentrations from other magmatic-hydrothermal mineralization systems (e.g., 20–200
540 ppm in the Coroccohuayco Fe-Cu-Au porphyry-skarn deposit, Peru; Chelle-Michou and
541 Chiaradia 2017).

542 Apatite composition data have been compiled from 14 porphyry (or skarn) Cu (or
543 Mo) or Fe-oxide copper-gold (IOCG) deposits and 7 barren systems. The corresponding
544 magma S concentrations have also been calculated based on the methods above (Fig. 11;
545 Appendix 10). In addition, melt inclusion composition data from 5 porphyry Mo (or Cu)
546 deposits and 4 barren igneous rocks have also been compiled in this study (Fig. 11;
547 Appendix 10). The available data together suggest that most of the ore-related magmas
548 contain similarly low magmatic S concentrations as the barren magmas. Moreover,
549 several smaller-sized deposits (e.g., Ouyangshan in Fig. 11) show similar or even slightly
550 higher magmatic S concentrations than some of the larger-sized deposits (e.g., Huojihe,
551 Tongchanggou, Luming, and Climax; Fig. 11). All these features suggest that the S
552 contents in the initial magmas associated with intrusion-related hydrothermal
553 mineralization are not necessarily as high as previously expected, despite some giant
554 deposits (e.g., the Bingham Canyon porphyry Cu deposit in Fig. 11) have been proved to
555 be relatively S-rich in the causative magma (e.g., Zhang and Audétat 2017b).

556 **Magma chamber volume and Mo content.** The S concentrations in the pre-degassing
557 melt determined above can be used to quantify the volume of the magma required to
558 release the S-bearing fluid accounting for the Huojihe Mo deposit (e.g., Chelle-Michou
559 and Chiaradia 2017). In Huojihe, there is a total Mo endowment of ca. 0.275 Mt (Tan et
560 al. 2013). Based on drill core logging and detailed observation, the molybdenite (MoS_2),
561 chalcopyrite ($CuFeS_2$), and pyrite (FeS_2) proportion can be estimated to be 2:1:2,

562 indicating a total of 0.275 Mt Mo, 0.138 Mt Cu, and 0.396 Mt Fe in the sulfides. There is
563 no other sulfide mineral like sphalerite or galena recognized in the mining area. Therefore,
564 a minimum of 0.635 Mt of reduced S (H_2S) is required for the precipitation of sulfide
565 minerals (i.e., 0.183 Mt S for molybdenite, 0.138 Mt S for chalcopyrite, and 0.314 Mt S
566 for pyrite). The reduced S could be supplied by SO_2 disproportionation and/or directly
567 from the magmatic H_2S after their degassing. In this study, the high oxidation state of the
568 Huojihe magma implies that the contents of H_2S from the magma could be far less than
569 the SO_2, and therefore all the reduced S required for sulfides could be reasonably
570 assumed to be formed by the disproportionation of SO_2 in the exsolved fluid from the
571 oxidized magma via the reaction of $4SO_2 + 4H_2O = H_2S + 3HSO_4^- + 3H^+$ (e.g.,
572 Kouzmanov and Pokrovski 2012). Accordingly at least 2.54 Mt of S are required to be
573 degassed from the magma. Given the S concentrations in the pre-degassing magma are
574 20–100 ppm as estimated above, a total mass of at least 2.54×10^4 to 12.7×10^4 Mt magma
575 would have been necessary to generate the S-bearing fluid. Assuming that the density of
576 the granitic melt is 2.62 g/cm^3, the magma chamber below the Huojihe deposit would
577 have been about 10–50 km^3.

578 A rough estimation of the Mo concentrations in the ore-related magma can be made
579 given the total Mo metal content (i.e., 0.275 Mt Mo) and the total mass of the magma
580 chamber (i.e., 2.54×10^4 to 12.7×10^4 Mt). The estimated Mo concentrations are 2–10 ppm,
581 which is similar to many other porphyry Mo mineralization systems (e.g., the Climax
582 porphyry Mo deposits, where Mo is generally <10 ppm with a maximum of 24 ppm) (Fig.
583 12a; Appendix 11). They are also comparable with many subeconomic Mo systems (3 to
584 32 ppm Mo), porphyry Cu mineralization systems (2 to 4.5 ppm Mo), and barren

585 magmatic systems (1.5 to 4 ppm Mo) (for details see Appendix 11). This suggests that a
586 high initial Mo content in the causative magma is not necessary for the generation of a
587 porphyry Mo deposit.

588

589 **IMPLICATIONS FOR THE FORMATION OF THE HUOJIHE PORPHYRY MO**
590 **DEPOSIT**

591 As has been previously proposed, porphyry deposits are genetically related to
592 magmas with a high oxygen fugacity, high water content, high S concentration, and high
593 metal contents (e.g., Burnham 1979; Lu et al. 2016; Richards et al. 2017). In this study,
594 although our data also support a relatively high magma oxygen fugacity in Huojihe, the
595 parental magma of the mineralized porphyry system is not unusually enriched in S (or
596 Mo). Therefore oxidized magmas may not always result in high magmatic S and metal
597 contents in porphyry systems. Nevertheless, the high oxygen fugacity might have played
598 a role as it could prevent Mo from dispersion into Ti-bearing magmatic minerals (e.g.,
599 titanite, magnetite, amphibole, and biotite) and retain it in the residual melt until fluid
600 exsolution, as Mo occurs mainly as Mo^{6+} in oxidized magmas rather than Mo^{4+}, and Mo^{6+}
601 is more incompatible with respect to Ti sites in magmatic minerals than Mo^{4+} (e.g.,
602 Candela and Bouton 1990; Černy et al. 2005; Shu et al. 2019).

603 The estimated magmatic Mo concentrations (2–10 ppm) are consistent with the low
604 Mo concentrations (0.15–0.33 ppm) in the magmatic zircons from the Huojihe biotite
605 monzogranite (Fig. 9; Appendix 5). It has been proposed by Lu et al. (2016) that zircons
606 from intrusions responsible for porphyry Mo mineralization commonly have higher Mo
607 concentrations (>1 ppm) than those in porphyry Cu or barren systems (<1 ppm) (Fig. 9).

608 However, in this study, the measured Mo concentrations in the zircons from the Huojihe
609 biotite monzogranite are relatively low (0.15–0.33 ppm), which is inconsistent with the
610 conclusions of Lu et al. (2016). The evidence presented above suggests that the Mo (and
611 also S) concentrations in magmas associated with economic porphyry Mo deposits are
612 not fundamentally different from subeconomic or barren magmas, which indicates that
613 the pre-degassing enrichment of Mo (and S) are not necessary for porphyry Mo
614 mineralization (e.g., Audétat 2010, 2015; Lerchbaumer and Audétat 2013; Mercer et al.
615 2015; Zhang and Audétat 2017a, b, 2018). This conclusion is also supported by the
616 results in Figs. 11 and 12a, in which porphyry Mo deposits with varying sizes have
617 similar S and Mo contents in their causative magmas.

618 A comparison between the calculated magma chamber volumes of several
619 porphyry Mo deposits with different sizes worldwide is presented in Fig. 12b and
620 summarized in Appendix 11. The data suggest that at least several tens to hundreds of
621 km^3 magma volumes are necessary to form a porphyry Mo deposit with a relatively large
622 size (e.g., >0.1 Mt), and that the magma volume generally increases with the increasing
623 metal tonnage of the generated porphyry Mo deposits (Fig. 12b). For two barren igneous
624 rocks (Rito del Medio and the Cañada Pinabete), geologically constrained magma
625 volumes (5 km^3) are too small to produce economic Mo deposits (Appendix 11).
626 Therefore, it is reasonable to come to the conclusion that magma chamber size could
627 have played an important role in the formation of an economic porphyry Mo deposit,
628 which is consistent with the results from Monte Carlo simulation of magma degassing by
629 Chelle-Michou et al. (2017).

630 However, there are also several other intrusions including the Drammen granite (60

631 km^3), the Glitrevann granite (30 km^3), and the Stronghold granite (80 km^3), which should
632 have been large enough to produce porphyry Mo deposits with >0.1 Mt Mo, but turn out
633 to be subeconomic or barren (Lerchbaumer and Audétat 2013). This suggests that factors
634 other than magma volume could also be of critical importance in the formation of Mo
635 mineralization. Likely candidates include (but are not limited to) the preservation of the
636 deposit, higher flux of magma, efficiency of Mo extraction from the magma, efficiency of
637 Mo precipitation, viscosity of the melt, and depth of magma chamber (e.g., Lerchbaumer
638 and Audétat 2013; Mercer et al. 2015; Yanites and Kesler 2015; Audétat and Li 2017;
639 Chelle-Michou et al. 2017; Zhang and Audétat 2017a, b).

640 To sum up, the current study demonstrates that magmatic accessory minerals
641 including zircon and apatite are useful to constrain the age, origin, and composition of the
642 magmas responsible for porphyry Mo mineralization. It is suggested that the
643 pre-degassing enrichment of S and Mo were not critically important in the formation of
644 the Huojihe Mo deposit, and that other factors, including (but not limited to) a large-sized
645 magma chamber, could also have played some key roles. This understanding might also
646 apply to other porphyry Mo deposits in NE China and worldwide.

647

648 ACKNOWLEDGMENTS

649 This study was made possible by financial support from the National Natural
650 Science Foundation of China (41973043 and 41873034), the MOST Special Fund from
651 the State Key Laboratory of Geological Processes and Mineral Resources, China
652 University of Geosciences (MSFGPMR201804), and the 111 Project of the Ministry of
653 Science and Technology (BP0719021). DL is supported by a NSERC Discovery grant.

We are grateful to Meijun Yang, Xiaolei Nie, Li Su, Chao Yu and Limin Zhou for their assistance during the analyses. We would also like to thank Daniel Harlov, Jun Deng, and Qingfei Wang for an earlier review and discussion that considerably improved the quality of the manuscript. This paper also benefited from the insightful reviews and comments by Cyril Chelle-Michou and an anonymous reviewer, and editorial handling by Gregory Dumond.

661 **REFERENCES CITED**

662 Audétat, A. (2010) Source and evolution of molybdenum in the porphyry-Mo (-Nb)
663 deposit at Cave Peak, Texas. Journal of Petrology, 51, 1739–1760.

664 Audétat, A. (2015) Compositional evolution and formation conditions of magmas and
665 fluids related to porphyry Mo mineralization at Climax, Colorado. Journal of
666 Petrology, 56, 1519–1546.

667 Audétat, A. (2019) The metal content of magmatic-hydrothermal fluids and its
668 relationship to mineralization potential. Economic Geology, 114, 1033–1056.

669 Audétat, A., and Li, W. (2017) The genesis of Climax-type porphyry Mo deposits:
670 insights from fluid inclusions and melt inclusions. Ore Geology Reviews, 88,
671 436–460.

672 Azadbakht, Z., Lentz, D.R., and McFarlane, C.R. (2018) Apatite chemical compositions
673 from Acadian-related granitoids of New Brunswick, Canada: implications for
674 petrogenesis and metallogenesis. Minerals, 8, 598.

675 Ballard, J.R., Palin, J.M., and Campbell, I.H. (2002) Relative oxidation states of magmas
676 inferred from Ce(IV)/Ce(III) in zircon: application to porphyry copper deposits of
677 Northern Chile. Contributions to Mineralogy and Petrology, 144, 347–364.

678 Belousova, E.A., Griffin, W.L., O'Reilly, S.Y., and Fisher, N.I. (2002a) Igneous zircon:
679 trace element composition as an indicator of source rock type. Contributions to
680 Mineralogy and Petrology, 143, 602–622.

681 Belousova, E.A., Griffin, W.L., O'Reilly, S.Y., and Fisher, N.I. (2002b) Apatite as an
682 indicator mineral for mineral exploration: trace-element composition and their
683 relationship to host rock type. Journal of Geochemical Exploration, 76, 45–69.

684 Blichert-Toft, J., and Albarède, F. (1997) The Lu-Hf isotope geochemistry of chondrites
685 and the evolution of the mantle-crust system. Earth and Planetary Science Letters,
686 148, 243–258.
687 Bouzari, F., Hart, C.J.R., Bissig, T., and Barker, S. (2016) Hydrothermal alteration
688 revealed by apatite luminescence and chemistry: a potential indicator mineral for
689 exploring covered porphyry copper deposits. Economic Geology, 111, 1397–1410.
690 Burnham, C.W. (1979) Magmas and hydrothermal fluids, *in* Barnes, H.L., ed.,
691 Geochemistry of hydrothermal ore deposits, 2nd edition. New York, John Wiley and
692 Sons, 71–136.
693 Candela, P.A. (1986) The evolution of aqueous vapor from silicate melts: Effect on
694 oxygen fugacity. Geochimica et Cosmochimica Acta, 50, 1205–1211.
695 Candela, P.A., and Bouton, S.L. (1990) The influence of oxygen fugacity on tungsten and
696 molybdenum partitioning between silicate melt and ilmenite. Economic Geology, 85,
697 633–640.
698 Cao, M.J., Li, G.M., Qin, K.Z., Seitmuratova, E.Y., and Liu, Y.S. (2012) Major and trace
699 element characteristics of apatites in granitoids from central Kazakhstan:
700 implications for petrogenesis and mineralization. Resource Geology, 62, 63–83.
701 Černy, P., Blevin, P.L., Cuney, M., and London, D. (2005) Granite-related ore deposits.
702 Economic Geology, 100th Anniversary Volume, 337–370.
703 Chelle-Michou, C., and Chiaradia, M. (2017) Amphibole and apatite insights into the
704 evolution and mass balance of Cl and S in magmas associated with porphyry copper
705 deposits. Contributions to Mineralogy and Petrology, 172, 105.
706 Chelle-Michou, C., Chiaradia, M., Ovtcharova, M., Ulianov, A., and Wotzlaw, J.F. (2014)

Zircon petrochronology reveals the temporal link between porphyry systems and the magmatic evolution of their hidden plutonic roots (the Eocene Coroccohuayco deposit, Peru). Lithos, 198–199, 129–140.

Chelle-Michou, C., Rottier, B., Caricchi, L., and Simpson, G. (2017) Tempo of magma degassing and the genesis of porphyry copper deposits. Scientific Reports, 1–12.

Chen, L., and Zhang, Y. (2018) In situ major-, trace-elements and Sr-Nd isotopic compositions of apatite from the Luming porphyry Mo deposit, NE China: constraints on the petrogenetic-metallogenic features. Ore Geology Reviews, 94, 93–103.

Chen, Y.J., Chen, Z., Wang, P., Pirajno, F., and Li N. (2017) The Mo deposits of Northeast China: a powerful indicator of tectonic settings and associated evolutionary trends. Ore Geology Reviews, 81, 602–640.

Cook, N., Ciobanu, C., George, L., and Ehrig, K. (2016) Trace element analysis of minerals in magmatic-hydrothermal ores by laser ablation inductively-coupled plasma mass spectrometry: approaches and opportunities. Minerals, 6, 1–34.

Coulson, I.M., Dipple, G.M., and Raudsepp, M. (2001) Evolution of HF and HCl activity in magmatic volatiles of the gold-mineralized Emerald Lake pluton, Yukon Territory, Canada. Mineral Deposita, 36, 594–606.

Deng, J., and Wang, Q.F. (2016) Gold mineralization in China: metallogenic provinces, deposit types and tectonic framework. Gondwana Research, 36, 219–274.

Deng, J., Wang, Q.F., and Li, G.J. (2017) Tectonic evolution, superimposed orogeny, and composite metallogenic system in China. Gondwana Research, 50, 216–266.

Dilles, J.H., Kent, A.J.R., Wooden, J.L., Tosdal, R.M., Koleszar, A., Lee, R.G., and

730 Farmer, L.P. (2015) Zircon compositional evidence for sulfur-degassing from
731 ore-forming arc magmas. Economic Geology, 110, 241–251.
732 Farmer, G.L., and DePaolo, D.J. (1984) Origin of Mesozoic and Tertiary granite in the
733 western United States and implications for pre-Mesozoic crustal structure, 2. Nd and
734 Sr isotopic studies of unmineralized and Cu- and Mo-mineralized granite in the
735 Precambrian craton. Journal of Geophysical Research, 89, 10141–10160.
736 Fei, X.H., Zhang, Z.C., Cheng, Z.G., Santosh, M., Jin, Z.L., Wen, B.B., Li, Z.X., and Xu,
737 L.J. (2018) Highly differentiated magmas linked with polymetallic mineralization: a
738 case study from the Cuihongshan granitic intrusions, Lesser Xing'an Range, NE
739 China. Lithos, 302–303, 158–177.
740 Fisher, C.M., Vervoort, J.D., and Hanchar, J.M. (2014) Guidelines for reporting zircon Hf
741 isotopic data by LA-MC-ICPMS and potential pitfalls in the interpretation of these
742 data. Chemical Geology, 363, 125–133.
743 Foster, G.L., and Vance, D. (2006) In situ Nd isotopic analysis of geological materials by
744 laser ablation MC-ICP-MS. Journal of Analytical Atomic Spectrometry, 21,
745 288–296.
746 Goldoff, B., Webster, J.D., and Harlov, D.E. (2012) Characterization of fluorchlorapatites
747 by electron probe microanalysis with a focus on time-dependent intensity variation
748 of halogens. American Mineralogist, 97, 1103–1115.
749 Griffin, W.L., Pearson, N.J., Belousova, E., Jackson, S.E., van Achterbergh, E., O'Reilly,
750 S.Y., and Shee, S.R., 2000. The Hf isotope composition of cratonic mantle:
751 LAM-MC-ICPMS analysis of zircon megacrysts in kimberlites. Geochimica et
752 Cosmochimica Acta, 64, 133–147.

753 Harlov, D.E. (2015) Apatite: a fingerprint for metasomatic processes. Elements, 11,
754 171–176.
755 Harlov, D.E., and Förster, H.J. (2003) Fluid-induced nucleation of (Y+REE)-phosphate
756 minerals within apatite: nature and experiment. Part II. Fluorapatite. American
757 Mineralogist, 88, 1209–1229.
758 Harlov, D.E., Wirth, R., and Förster, H. (2005) An experimental study of dissolution
759 reprecipitation in fluorapatite: fluid infiltration and the formation of monazite.
760 Contributions to Mineralogy and Petrology, 150, 268–286.
761 Henry, D.J., Guidotti, C.V., and Thomson, J.A. (2005) The Ti-saturation surface for low
762 to medium pressure metapelitic biotite: implications for geothermometry and
763 Ti-substitution mechanisms. American Mineralogist, 90, 316–328.
764 Hu, X.L., Ding, Z.J., He, M.C., Yao, S.Z., Zhu, B.P., Shen, J., and Chen, B. (2014) A
765 porphyry-skarn metallogenic system in the Lesser Xing'an Range, NE China:
766 implications from U-Pb and Re-Os geochronology and Sr-Nd-Hf isotopes of the
767 Luming Mo and Xulaojiugou Pb-Zn deposits. Journal of Asian Earth Sciences, 90,
768 88–100.
769 Hu, X.L., Yao, S.Z., Zeng, G.P., Liu, W.H., and Zhang, Z.J. (2019) Multistage magmatism
770 resulting in large-scale mineralization: a case from the Huojihe porphyry Mo deposit
771 in NE China. Lithos, 326–327, 397–414.
772 Jahn, B.M., Cornichet, J., Cong, B.L., and Yui, T.F. (1996) Ultrahigh-ε_{Nd} eclogites from
773 an ultrahigh-pressure metamorphic terrane of China. Chemical Geology, 127, 61–
774 79.
775 Ketcham, R.A. (2015) Technical Note: calculation of stoichiometry from EMP data for

776 apatite and other phases with mixing on monovalent anion sites. American
777 Mineralogist, 100, 1620–1623.
778 Keto, L.S., and Jacobsen, S.B. (1987) Nd and Sr isotopic variations of Early Paleozoic
779 oceans. Earth and Planetary Science Letters, 84, 27–41.
780 Klemm, L.M., Pettke, T., and Heinrich, C.A. (2008) Fluid and source magma evolution of
781 the Questa porphyry Mo deposit, New Mexico, USA. Mineralium Deposita, 43,
782 533–552.
783 Konecke, B.A., Fiege, A., Simon, A.C., Parat, F., and Stechern, A. (2017) Covariability of
784 S^{6+}, S^{4+}, and S^{2-} in apatite as a function of oxidation state: implications for a new
785 oxybarometer. American Mineralogist, 102, 548–557.
786 Kouzmanov, K., and Pokrovski, G.S. (2012) Hydrothermal controls on metal distribution
787 in porphyry Cu (-Mo-Au) systems. Special Publication of the Society of Economic
788 Geologists, 16, 573–618.
789 Lerchbaumer, L., and Audétat, A. (2013) The metal content of silicate melts and aqueous
790 fluids in subeconomically Mo mineralized granites: implications for porphyry Mo
791 genesis. Economic Geology, 108, 987–1013.
792 Li, X.C., and Zhou, M.F. (2015) Multiple stages of hydrothermal REE remobilization
793 recorded in fluorapatite in the Paleoproterozoic Yinachang Fe-Cu-(REE) deposit,
794 Southwest China. Geochimica et Cosmochimica Acta, 166, 53–73.
795 Liu, W.G., Liu, H., Li, G.Z., Zhou, H.Y., Xiao, Z.B., Tu, J.R., and Li, H.M. (2017) The
796 application of ion exchange resins in Sr-Nd isotopic assay of geological samples.
797 Acta Geologica Sinica, 91, 2584–2592 (in Chinese with English abstract).
798 Liu, Y., Hu, Z., Gao, S., Günther, D., Xu, J., Gao, C., and Chen, H. (2008) In situ analysis

799 of major and trace elements of anhydrous minerals by LA-ICP-MS without applying
800 an internal standard. Chemical Geology, 257, 34–43.
801 Loader, M.A., Wilkinson, J.J., and Armstrong, R.N. (2017) The effect of titanite
802 crystallisation on Eu and Ce anomalies in zircon and its implications for the
803 assessment of porphyry Cu deposit fertility. Earth and Planetary Science Letters, 472,
804 107–119.
805 Lu, Y.J., Loucks, R.R., Fiorentini, M., McCuaig T.C., Evans, N.J., Yang, Z.M., Hou, Z.Q.,
806 Kirkland, C.L., Parra-Avila, L.A., and Kobussen, A. (2016) Zircon compositions as
807 a pathfinder for porphyry Cu ± Mo ± Au deposits. Society of Economic Geologists
808 Special Publication, 19, 329–347.
809 Ludwig, K.R. (2003) User's Manual for Isoplot 3.0: a geochronological Toolkit for
810 Microsoft Excel. Berkeley Geochronology Center Special Publication, 4, 71.
811 Mathez, E.A., and Webster, J.D. (2005) Partitioning behavior of chlorine and fluorine in
812 the system apatite-silicate melt-fluid. Geochimica et Cosmochimica Acta, 69,
813 1275–1286.
814 Mercer, C.N., Hofstra, A.H., Todorov, T.I., Roberge, J., Burgisser, A., Adams, D.T., and
815 Cosca, M. (2015) Pre-eruptive conditions of the Hideaway Park topaz rhyolite:
816 insights into metal source and evolution of magma parental to the Henderson
817 porphyry molybdenum deposit, Colorado. Journal of Petrology, 56, 645–679.
818 Ouyang, H.G., Mao, J.W., Santosh, M., Zhou, J., Zhou, Z.H., and Wu, Y. (2013)
819 Geodynamic setting of Mesozoic magmatism in NE China and surrounding regions:
820 perspectives from spatio-temporal distribution patterns of ore deposits. Journal of
821 Asian Earth Sciences, 78, 222–236.

822 Pan, L.C., Hu, R.Z., Wang, X.S., Bi, X.W., Zhu, J.J., and Li, C. (2016) Apatite trace
823 element and halogen compositions as petrogenetic-metallogenic indicators:
824 examples from four granite plutons in the Sanjiang region, SW China. Lithos, 254,
825 118–130.
826 Pan, Y., and Fleet, M.E. (2002) Compositions of the apatite group minerals: substitution
827 mechanisms and controlling factors. Reviews in Mineralogy, 48, 13–49.
828 Parat, F., Holtz, F., and Klügel, A. (2011) S-rich apatite-hosted glass inclusions in
829 xenoliths from La Palma: constraints on the volatile partitioning in evolved alkaline
830 magmas. Contributions to Mineralogy and Petrology, 162, 463–478.
831 Paton C., Woodhead J.D., Hellstrom J.C., Hergt J.M., Greig A., and Maas R. (2010)
832 Improved laser ablation U-Pb zircon geochronology through robust downhole
833 fractionation correction. Geochemistry Geophysics Geosystems, 11, 1–36.
834 Peng, G.Y., Juhr, J.F., and McGee, J.J. (1997) Factors controlling sulfur concentrations in
835 volcanic apatite. American Mineralogist, 82, 1210–1224.
836 Piccoli, P.M., and Candela, P.A. (2002) Apatite in igneous systems. Reviews in
837 Mineralogy and Geochemistry, 48, 255–292.
838 Prowatke, S., and Klemme, S. (2006) Trace element partitioning between apatite and
839 silicate melts. Geochimica et Cosmochimica Acta, 70, 4513–4527.
840 Putnis, A. (2009) Mineral replacement reactions. Reviews in Mineralogy and
841 Geochemistry, 70, 87–124.
842 Pyle, J.M., Spear, F.S., and Wark, D.A. (2002) Electron microprobe analysis of REE in
843 apatite, monazite and xenotime: protocols and pitfalls. In: Kohn, M.L., Rakovan, J.
844 & Hughes, J.M. (eds), Phosphates-Geochemical, Geobiological, and Materials

Importance. Mineralogical Society of America and Geochemical Society, Reviews in Mineralogy and Geochemistry, 48, 337–362.

Ren, L., Sun, J.G., Han, J.G., Liu, Y., Wang, C.S., Gu, A.L., Zhao, K.Q., and Yu, R.D. (2017) Magmatism and metallogenic mechanisms of the Baoshan Cu-polymetallic deposit from the Lesser Xing'an Range, NE China: constraints from geology, geochronology, geochemistry, and Hf isotopes. Ore Geology Reviews, 88, 270–288.

Richards, J.P. (2009) Postsubduction porphyry Cu-Au and epithermal Au deposits: products of remelting of subduction-modified lithosphere. Geology, 37, 247–250.

Richards, J.P., López, G.P., Zhu, J.J., Creaser, R.A., Locock, A.J., and Mumin, A.H. (2017) Contrasting tectonic settings and sulfur contents of magmas associated with Cretaceous porphyry Cu ± Mo ± Au and intrusion-related iron oxide Cu-Au deposits in northern Chile. Economic Geology, 112, 295–318.

Scherer, E., Munker, C., and Mezger, K. (2001) Calibration of the lutetium-hafnium clock. Science, 293, 683–686.

Sengör, A.M.C., and Natal'in, B.A. (1996) Paleotectonics of Asia: fragments of a synthesis. In: Yin, A., Harrison, M. (Eds.), The Tectonic Evolution of Asia. Cambridge University Press, 486–640.

Sha, L.K., and Chappell, B.W. (1999) Apatite chemical composition, determined by electron microprobe and laser-ablation inductively coupled plasma mass spectrometry, as a probe into granite petrogenesis-some mineralogical and petrological constraints. Geochimica et Cosmochimica Acta, 63, 3861–3881.

Shen, P., Hattori, K., Pan, H., Jackson, S., and Seitmuratova, E. (2015) Oxidation condition and metal fertility of granitic magmas: zircon trace element data from

porphyry Cu deposits in the Central Asian Orogenic Belt. Economic Geology, 110, 1861–1878.

Shu, Q., Chang, Z., Lai, Y., Zhou, Y., Sun, Y., and Yan, C. (2016) Regional metallogeny of Mo-bearing deposits in northeastern China, with new Re-Os dates of porphyry Mo deposits in the northern Xilamulun district. Economic Geology, 111, 1783–1798.

Shu, Q., Chang, Z., Lai Y., Hu, X., Wu, H., Zhang, Y., Wang, P., Zhai, D., and Zhang, C. (2019) Zircon trace elements and magma fertility: insights from porphyry (-skarn) Mo deposits in NE China. Mineralium Deposita, 54, 645–656.

Sillitoe, R.H., and Hedenquist, J.W. (2003) Linkages between volcanotectonic settings, ore-fluid compositions, and epithermal precious metal deposits. Society of Economic Geologists Special Publication, 10, 315–343.

Stock, M.J., Humphreys, M.C.S., Smith, V.C., Isaia, R., Brooker, R.A., and Pyle, D.M. (2018) Tracking volatile behaviour in sub-volcanic plumbing systems using apatite and glass: insights into pre-eruptive processes at Campi Flegrei, Italy. Journal of Petrology, 59, 2463–2492.

Stock, M. J., Humphreys, M.C.S., Smith, V.C., Johnson, R.D., Pyle, D.M., and EIMF (2015). New constraints on electron-beam induced halogen migration in apatite. American Mineralogist, 100, 281–293.

Stormer, J.C., Pierson, M.L., and Tacker, R.C. (1993). Variation of F and Cl X-ray intensity due to anisotropic diffusion in apatite. American Mineralogist, 78, 641–648.

Streck, M.J., and Dilles, J.H. (1998) Sulfur evolution of oxidized arc magmas as recorded in apatite from a porphyry copper batholith. Geology, 26, 523–526.

Sun, J.G., Zhang, Y., Xing, S.W., Zhao, K.Q., Zhang, Z.J., Bai, L.A., Ma, Y.B., and Liu, Y.S. (2012) Genetic types, ore-forming age and geodynamic setting of endogenic molybdenum deposits in the eastern edge of Xing-Meng orogenic belt. Acta Petrologica Sinica, 16, 1317–1332 (in Chinese with English abstract).

Tan, H.Y., Wang, D.D., Lu, J.C., Shu, G.L., and Han, R.P. (2013) Petrogenesis and mineralization chronology study on the Huojihe molybdenum deposit Xiao Hinggan Mountains and its geological implication. Acta Petrologica et Mineralogica, 32, 733–750 (in Chinese with English abstract).

Vervoort, J.D., and Blichert-Toft, J. (1999) Evolution of the depleted mantle: Hf isotope evidence from juvenile rocks through time. Geochimica et Cosmochimica Acta, 63, 553–556.

Wang, F., Xu, W.L., Gao, F.H., Zhang, H.H., Pei, F.P., Zhao, L., and Yang, Y. (2014) Precambrian terrane within the Songnen-Zhangguangcai Range Massif, NE China: evidence from U-Pb ages of detrital zircons from the Dongfengshan and Tadong groups. Gondwana Research, 26, 402–413.

Wang, F.Y., Ge, C., Ning, S.Y., Nie, L.Q., Zhong, G.X., and Noel, C.W. (2017) A new approach to LA-ICP-MS mapping and application in geology. Acta Petrologica Sinica, 33, 3422–3436 (in Chinese with English abstract).

Watson, E.B. (1980) Apatite and phosphorus in mantle source regions: an experimental study of apatite/melt equilibria at pressures to 25 kbar. Earth and Planetary Science Letters, 51, 322–335.

Wu, F.Y., Jahn, B.M., Wilde, S.A., Lo, C.H., Yui, T.F., Lin, Q., Ge, W.C., and Sun, D.Y. (2003) Highly fractionated I-type granites in NE China (II): isotopic geochemistry

914 and implications for crustal growth in the Phanerozoic. Lithos, 67, 191– 204.
915 Wu, F.Y., Jahn, B.M., Wilde, S.A., and Sun, D.Y. (2000) Phanerozoic crustal growth:
916 U-Pb and Sr-Nd isotopic evidence from the granites in northeastern China.
917 Tectonophysics, 328, 89–113.
918 Wu, F.Y., Sun, D.Y., Ge, W.C., Zhang, Y.B., Grant, M.L., Wilde, S.A., and Jahn, B.M.
919 (2011) Geochronology of the Phanerozoic granitoids in northeastern China. Journal
920 of Asian Earth Sciences, 41, 1–30.
921 Yang, Y.C., Han, S.J., Sun, D.Y., Guo, J., and Zhang, S.J. (2012) Geological and
922 geochemical features and geochronology of porphyry molybdenum deposits in the
923 Lesser Xing'an Range-Zhangguangcai Range metallogenic belt. Acta Petrologica
924 Sinica, 28, 379–390 (in Chinese with English abstract).
925 Yanites, B.J., and Kesler, S.E. (2015) A climate signal in exhumation patterns revealed by
926 porphyry copper deposits. Nature Geoscience, 8, 462–465.
927 Zeng, L.P., Zhao, X.F., Li, X.C., Hu, H., and McFarlane, C. (2016) In situ elemental and
928 isotopic analysis of fluorapatite from the Taocun magnetite-apatite deposit, Eastern
929 China: constraints on fluid metasomatism. American Mineralogist, 101, 2468–2483.
930 Zhai, D.G., Liu, J.J., Tombros, S., and Williams-Jones, A.E. (2018) The genesis of the
931 Hashitu porphyry molybdenum deposit, Inner Mongolia, NE China: constraints from
932 mineralogical, fluid inclusion, and multiple isotope (H, O, S, Mo, Pb) studies.
933 Mineralium Deposita, 53, 377–397.
934 Zhang, D., and Audétat, A. (2017a) Chemistry, mineralogy and crystallization conditions
935 of porphyry Mo-forming magmas at Urad-Henderson and Silver Creek, Colorado,
936 USA. Journal of Petrology, 58, 277–296.

937 Zhang, D., and Audétat, A. (2017b) What caused the formation of the giant Bingham
938 Canyon porphyry Cu-Mo-Au deposit? Insights from melt inclusions and magmatic
939 sulfides. Economic Geology, 112, 221–244.
940 Zhang, D., and Audétat, A. (2018) Magmatic-hydrothermal evolution of the barren
941 Huangshan pluton, Anhui Province, China: a melt and fluid inclusion study.
942 Economic Geology, 113, 803–824.
943 Zhang, J.H., Gao, S., Ge, W.C., Wu, F.Y., Yang, J.H., Wilde, S.A., and Li, M. (2010)
944 Geochronology of the Mesozoic volcanic rocks in the Great Xing'an Range,
945 northeastern China: implications for subduction-induced delamination. Chemical
946 Geology, 276, 144–165.
947 Zhang, L.L., Liu, C., Zhou, S., Sun, K., Qin, R.Z., and Feng, Y. (2014) Characteristics of
948 ore-bearing granites and ore-forming age of the Huojihe molybdenum deposit in
949 Lesser Xing'an Range. Acta Petrologica Sinca, 30, 3419–3431 (in Chinese with
950 English abstract).
951 Zhang, Y.M., Gu, X.X., Liu, R.P., Sun, X., Li, X.L., and Zheng, L. (2017) Geology,
952 geochronology and geochemistry of the Gaogangshan Mo deposit: a newly
953 discovered Permo-Triassic collision-type Mo mineralization in the Lesser Xing'an
954 Range, NE China. Ore Geology Reviews, 81, 672–688.
955 Zhao, X.F., Zhou, M.F., Gao, J.F., Li, X.C., and Li, J.W. (2015) In situ Sr isotope analysis
956 of apatite by LA-MC-ICPMS: constraints on the evolution of ore fluids of the
957 Yinachang Fe-Cu-REE deposit, Southwest China. Mineralium Deposita, 50,
958 871–884.

959 Zhu, J.J., Richards, J.P., Rees, C., Creaser, R., DuFrane, S.A., Locock, A., Petrus, J.A.,
960 and Lang, J. (2018) Elevated magmatic sulfur and chlorine contents in ore-forming
961 magmas at the Red Chris porphyry Cu-Au deposit, northern British Columbia,
962 Canada. Economic Geology, 113, 1047–1075.
963 Zindler, A., Jagoutz, E., and Goldstein, S. (1982) Nd, Sr and Pb isotopic systematics in a
964 three-component mantle: a new perspective. Nature, 298, 519–523.
965

This is a preprint, the final version is subject to change, of the American Mineralogist (MSA)
Cite as Authors (Year) Title. American Mineralogist, in press.
DOI: https://doi.org/10.2138/am-2020-7226

966 # Figure captions

967 **Fig. 1** (a) Tectonic framework of northeastern China, modified after Wu et al. (2011); (b)
968 Simplified geological map of the Lesser Xing'an Range region, showing the distribution
969 of major porphyry Mo, epithermal Au, and skarn deposits (modified after Ren et al.
970 2017).

971 **Fig. 2** (a) Geological map of the Huojihe porphyry Mo deposit, modified after Yang et al.
972 (2012). (b) Cross section of the prospecting line 7 of the Huojihe deposit showing the
973 collected sample locations (modified after Hu et al. 2019).

974 **Fig. 3** Hand specimen photographs (a, b, c) and photomicrographs (d, e, f) of the
975 intrusions and ores from the Huojihe deposit. (a) Granodiorite; (b) Quartz-molybdenite
976 vein and disseminated chalcopyrite in the biotite monzogranite; (c) Quartz-molybdenite
977 vein with K-feldspar halos in the biotite monzogranite; (d) Biotite monzogranite; (e)
978 Quartz-molybdenite vein with K-feldspar halos in the granodiorite; (f)
979 Quartz-molybdenite vein. Abbreviations: Bi = biotite; Cpy = chalcopyrite; Kfs =
980 K-feldspar; Mol = molybdenite; Pl = plagioclase; Qtz = quartz.

981 **Fig. 4** Plot of $(^{87}Sr/^{86}Sr)_i$ vs. $\varepsilon_{Nd}(t)$ for whole rock and apatite samples from the Huojihe
982 granitoids and several other porphyry/skarn Mo-bearing deposits in the Lesser Xing'an
983 Range region. The complied whole rock Sr-Nd isotopic compositions of porphyry/skarn
984 Mo-bearing deposits include Cuihongshan (Fei et al. 2018), Luming, and Xulaojiugou
985 (Hu et al. 2014). The shaded area of the granitoids in northeastern China is from Wu et al.
986 (2003), and the brown area of the depleted mantle is from Zindler et al. (1982).

987 **Fig. 5** Transmitted (a, b, c, d), optical microscopic cathodoluminescence (e, f) and back

scattered electron (g, h, i) images of representative apatites. (a) Transmitted microscopic photos of euhedral to subhedral apatite grains occurring as inclusions within biotite; (b, c, d) Transmitted, microscopic photos of Ap_m and Ap_h. Note that Ap_m is inclusion-free and transparent, whereas Ap_h often partly or completely replaces Ap_m with an irregular, altered crystal shape; (e, f) Optical microscopic cathodoluminescence images of Ap_m and Ap_h. Note that Ap_m has a homogeneous yellow luminescence, whereas Ap_h displays an imbalanced light yellow-green luminescence; (g, h, i) Backscattered electron images of Ap_m and Ap_h. Note that Ap_m has oscillatory zoning and core-rim textures, and was hydrothermally altered into Ap_h at the rim. Ap_h has many voids and monazite mineral inclusions. Ap_m is bright and homogeneous, whereas Ap_h has darker color. Abbreviations: Bi = biotite; Ep = epidote; FI = fluid inclusion; Mnz = monazite; Pl = plagioclase; Qtz = quartz.

Fig. 6 Plots of geochemical compositions of Ap_m and Ap_h from the Huojihe deposit. Plots of (a) Ca (apfu) vs. Mn (apfu), (b) Ca (apfu) vs. Cl (apfu), (c) Nd (ppm) vs. Ce (ppm), (d) Y (ppm) vs. Ce (ppm), (e) MnO (wt %) vs. total REE + Y, and (f) Chondrite-normalized rare earth element distribution patterns of apatites. apfu = atoms per formula unit.

Fig. 7 (a) Zircon concordia plots of the biotite monzogranite from the Huojihe deposit. (b) Cathodoluminescence images of representative zircon grains from the Huojihe biotite monzogranite with $^{206}Pb/^{238}U$ ages and $\varepsilon_{Hf}(t)$ values for each analyzed spot.

Fig. 8 Plots of (a) apatite δEu vs. δCe, (b) apatite Ga (ppm) vs. δEu, and (c) zircon δEu vs. δCe. For apatite, the complied porphyry Mo deposits include Tongchanggou, Xiuwacu, Luming, and Luoboling. The compiled porphyry/skarn Cu-(Au-Pb-Zn) deposits include Weibao, Pulang, Baoshan, and Tongshanling. The compiled barren igneous rocks include

the barren Weibao diorite porphyry, the barren Triassic Xiuwacu pluton, and the barren Zhongliao porphyritic granodiorite from Luoboling. For zircon, the complied porphyry Mo-bearing deposits include Sungun, Sar Cheshmeh, Jiama, Qulong, Yuchiling, Nannihu, and Dexing. The complied porphyry Cu-Au deposits include Tampakan and Batu Hijau. The compiled barren igneous rocks include the Bandelier rhyolite, the Lucerne reduced granite, the Yellowstone rhyolite, the Kadoona I-type dacite, the Hawkins S-type dacite, and the Bishop Tuff rhyolite. Data details are listed in Appendix 9.

Fig. 9 Plot of Eu_N/Eu_N* vs. Mo (ppm) in zircons from Huojihe. Also shown for comparison are compiled zircons from other porphyry deposits and barren igneous rocks. The porphyry Mo-bearing deposits include Sungun, Sar Cheshmeh, Jiama, Qulong, Yuchiling, Nannihu, and Dexing. The complied porphyry Cu-Au deposits include Tampakan and Batu Hijau. The complied barren igneous rocks include the Bandelier rhyolite, the Lucerne reduced granite, the Yellowstone rhyolite, the Kadoona I-type dacite, the Hawkins S-type dacite, and the Bishop Tuff rhyolite. All these data are from Lu et al. (2016) and can be found in Appendix 9.

Fig. 10 Plot of U-Pb ages vs. $\varepsilon_{Hf}(t)$ in zircons from Huojihe and several other porphyry/ skarn Mo and Au deposits in the Lesser Xing'an Range region. Compiled details of the zircon data are listed in Appendix 5.

Fig. 11 Plot of metal tonnage of several porphyry, skarn, and Fe-oxide Cu-Au deposits and barren igneous rocks vs. magmatic S concentrations as determined by apatites or directly measured from melt inclusions. In (a), the magmatic S concentrations were estimated using the temperature-dependent apatite-melt partition coefficient formula of Peng et al. (1997): $\ln K_D = 21{,}130/T-16.2$ (where T is in Kelvin, K_D is the fluid/melt

partition coefficient for S). In (b) the magmatic S concentrations were estimated using the apatite-melt partition coefficient formula of Parat et al. (2011): SO_3 apatite (wt %) = 0.157 × ln[SO_3] (melt, wt %) + 0.9834. The squares represent the median magmatic S concentrations for each deposit or barren igneous rock. The compiled data are listed in Appendix 10.

Fig. 12 (a) Plot of metal tonnage vs. magmatic Mo concentrations of Huojihe and several other porphyry Mo deposits. (b) Plot of metal tonnage vs. estimated magma volumes of Huojihe and several other porphyry Mo deposits. The compiled data are listed in Appendix 11.

This is a preprint, the final version is subject to change, of the American Mineralogist (MSA)
Cite as Authors (Year) Title. American Mineralogist, in press.
DOI: https://doi.org/10.2138/am-2020-7226

Electronic supplementary material

Appendix 1 General description of the related granitic samples from the Huojihe deposit used for analyses, and whole rock major (in wt %) and trace element (in ppm) compositions of granitic samples from the Huojihe porphyry Mo deposit.

Appendix 2 Primitive mantle-normalized trace element patterns for the Huojihe granitic samples.

Appendix 3 Sr-Nd isotopic compositions of granitic samples from the Huojihe deposit and three other porphyry/skarn Mo-bearing deposits in the Lesser Xing'an region (Luming, Cuihongshan and Xulaojiugou).

Appendix 4 Full dataset of apatite major (in wt %) and trace element (in ppm) compositions and Sr-Nd isotopic compositions, and calculated apatite ΣREE, δEu, δCe, X_F/X_{OH}, X_F/X_{Cl}, X_{Cl}/X_{OH}, and apfu values from the Huojihe deposit.

Appendix 5 Full dataset of zircon U-Pb ages and trace element abundances (in ppm) from the biotite monzogranite in the Huojihe deposit. Also shown are the zircon Hf isotopic compositions of the igneous rocks from Huojihe, four porphyry/skarn Mo-bearing and three Au deposits in Lesser Xing'an region.

Appendix 6 Full dataset of biotite major element compositions (in wt %), and calculated biotite apfu values, X_{Mg} values, and precipitation temperatures (°C) from the Huojihe deposit.

Appendix 7 Plots of (a) SiO_2 vs. ($Na_2O + K_2O$), (b) SiO_2 vs. K_2O, (c) A/CNK [molar ratio $Al_2O_3/(CaO + Na_2O + K_2O)$] vs. A/NK [molar ratio $Al_2O_3/(Na_2O + K_2O)$], (d)

1064 10000Ga/Al vs. (Na_2O + K_2O), and (e) Zr + Nb + Ce + Y vs. (Na_2O + K_2O)/CaO
1065 diagrams for Huojihe granitic samples.

1066 **Appendix 8** Plot of X_F/X_{OH} vs. X_{Cl}/X_{OH} ratios of biotite-hosted apatite inclusion
1067 compositions.

1068 **Appendix 9** A summary of the partial apatite and zircon trace element abundances (in
1069 ppm) and calculated δEu, δCe values for Huojihe, compiled porphyry Mo-bearing and
1070 Cu-(Au-Pb-Zn) deposits and barren igneous rocks.

1071 **Appendix 10** A summary of magmatic S concentrations determined by apatites SO_3
1072 (calculated using two methods) or directly measured by melt inclusions and metal
1073 tonnage for Huojihe and the compiled 19 porphyry/skarn/Fe-oxide Cu-Au deposits and
1074 11 barren igneous rocks.

1075 **Appendix 11** A summary of metal tonnage, magmatic Mo concentrations and estimated
1076 magma volume for Huojihe and compiled porphyry Mo deposits, subeconomic Mo
1077 mineralization, porphyry Cu (-Mo, Au) deposits, and barren igneous rocks.

Figure 1

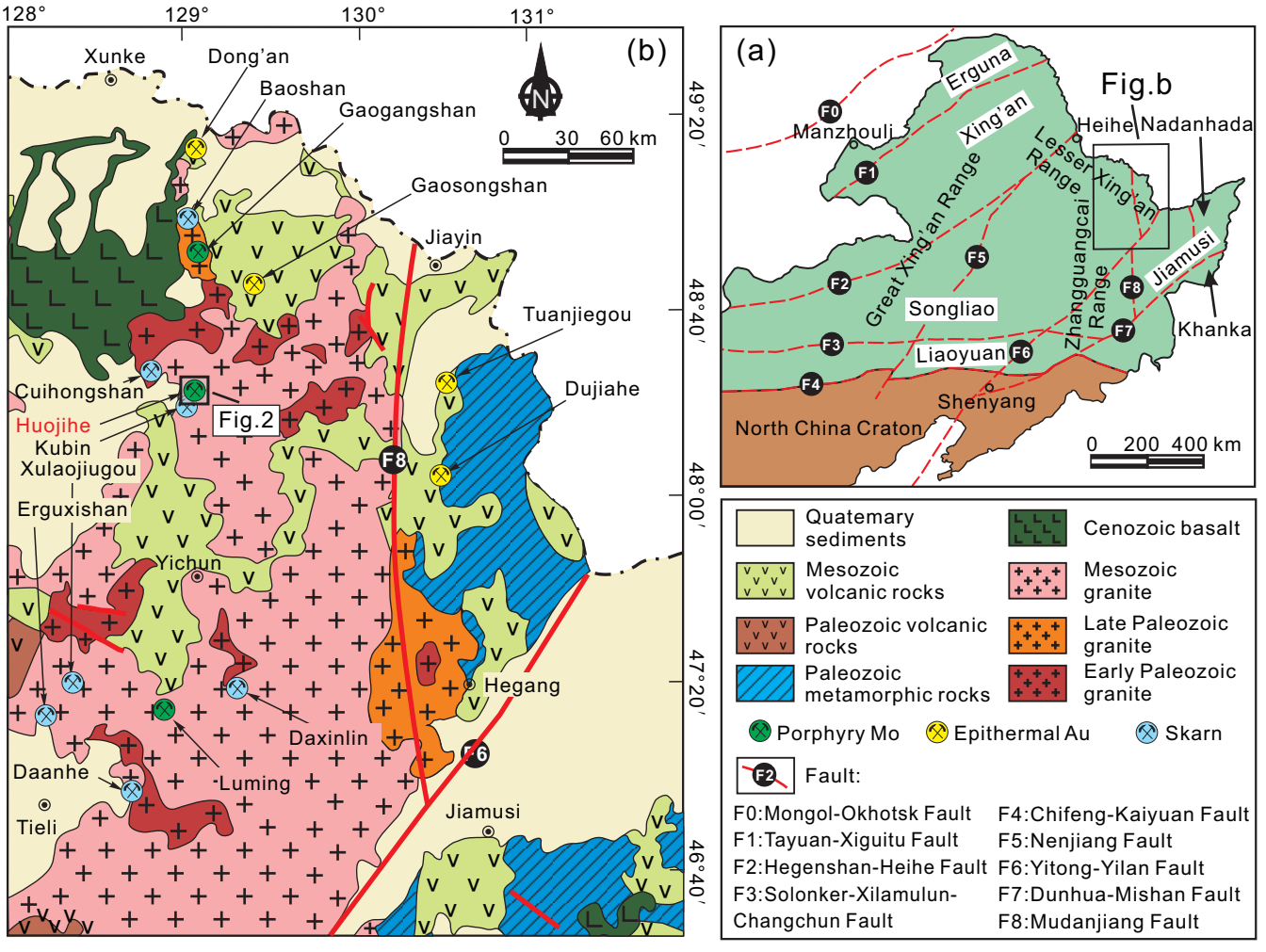
128°
129°
130°
131°
49°20′
48°40′
48°00′
47°20′
46°40′
(b)
N
0 30 60 km
Xunke
Dong'an
Baoshan
Gaogangshan
Gaosongshan
Jiayin
Tuanjiegou
Dujiahe
Cuihongshan
Huojihe
Kubin
Xulaojiugou
Fig.2
Erguxishan
Yichun
Hegang
Daxinlin
Daanhe
Luming
Tieli
Jiamusi
F8
F6
(a)
Fig.b
Erguna
Xing'an
Manzhouli
Heihe
Nadanhada
Lesser Xing'an Range
Great Xing'an Range
Zhangguangcai Range
Songliao
Liaoyuan
Shenyang
North China Craton
Jiamusi
Khanka
F0
F1
F2
F3
F4
F5
F6
F7
F8
0 200 400 km
Quaternary sediments
Cenozoic basalt
Mesozoic volcanic rocks
Mesozoic granite
Paleozoic volcanic rocks
Late Paleozoic granite
Paleozoic metamorphic rocks
Early Paleozoic granite
Porphyry Mo
Epithermal Au
Skarn
Fault:
F0:Mongol-Okhotsk Fault
F1:Tayuan-Xiguitu Fault
F2:Hegenshan-Heihe Fault
F3:Solonker-Xilamulun-Changchun Fault
F4:Chifeng-Kaiyuan Fault
F5:Nenjiang Fault
F6:Yitong-Yilan Fault
F7:Dunhua-Mishan Fault
F8:Mudanjiang Fault

Figure 2

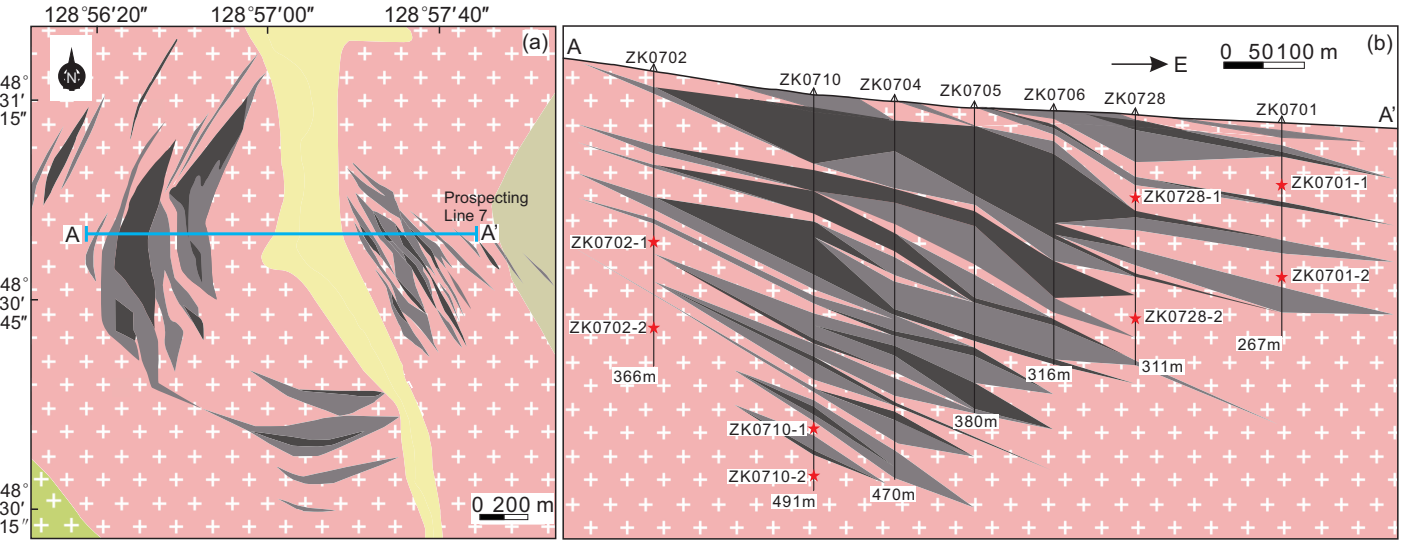

Quaternary | Permian Wudaoling Formation volcanic rocks | Jurassic granitoids | Jurassic alkali-feldspar granite | High-grade primary orebody (Mo≥0.06%)

Low-grade primary orebody (Mo: 0.03%~0.06%) | ZK0701 Drill core and number | 366m Depth of drill core | ★ZK0701 Location and number of sample | Prospecting line

Figure 3

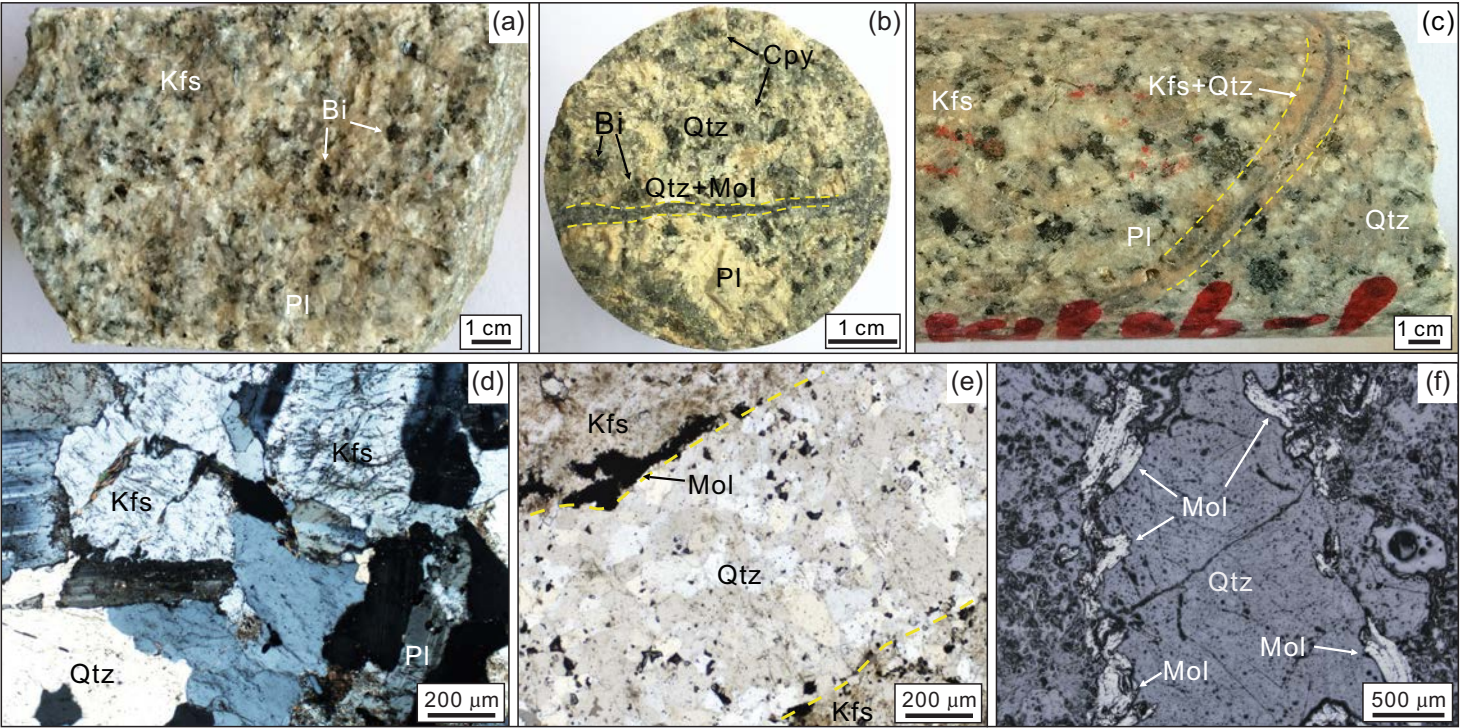
(a)
Kfs
Bi
Pl
1 cm
(b)
Cpy
Bi
Qtz
Qtz+Mol
Pl
1 cm
(c)
Kfs
Kfs+Qtz
Pl
Qtz
1 cm
(d)
Kfs
Kfs
Qtz
Pl
200 μm
(e)
Kfs
Mol
Qtz
Kfs
200 μm
(f)
Mol
Qtz
Mol
Mol
500 μm

Figure 4

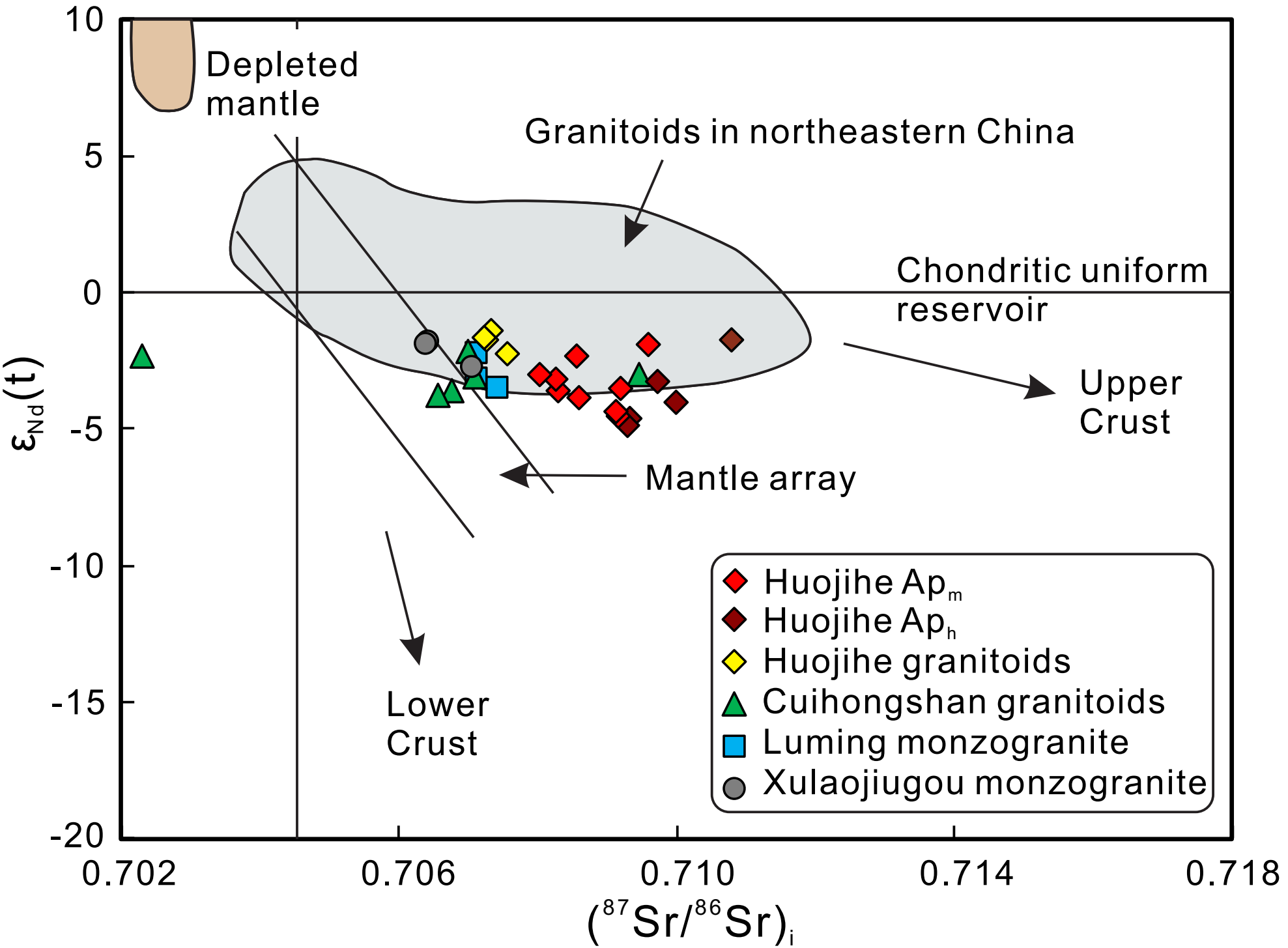
10
5
0
-5
-10
-15
-20
0.702
0.706
0.710
0.714
0.718
$\varepsilon_{Nd}(t)$
$(^{87}Sr/^{86}Sr)_i$
Depleted mantle
Granitoids in northeastern China
Chondritic uniform reservoir
Upper Crust
Mantle array
Lower Crust
Huojihe Ap_m
Huojihe Ap_h
Huojihe granitoids
Cuihongshan granitoids
Luming monzogranite
Xulaojiugou monzogranite

Figure 5

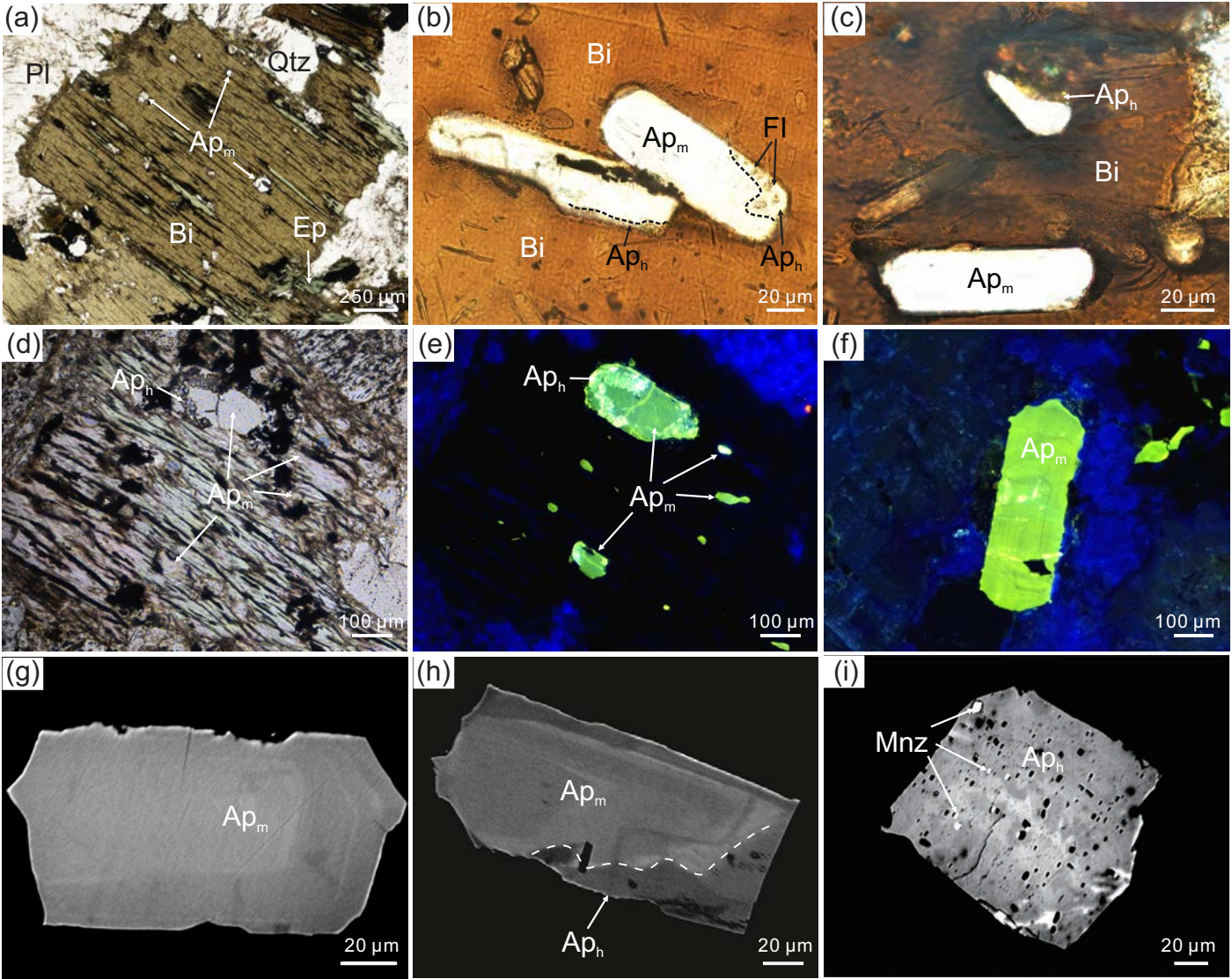
(a)
Pl
Qtz
Ap$_m$
Bi
Ep
250 μm
(b)
Bi
Ap$_m$
Fl
Bi
Ap$_h$
Ap$_h$
20 μm
(c)
Ap$_h$
Bi
Ap$_m$
20 μm
(d)
Ap$_h$
Ap$_m$
100 μm
(e)
Ap$_h$
Ap$_m$
100 μm
(f)
Ap$_m$
100 μm
(g)
Ap$_m$
20 μm
(h)
Ap$_m$
Ap$_h$
20 μm
(i)
Mnz
Ap$_h$
20 μm

Figure 6

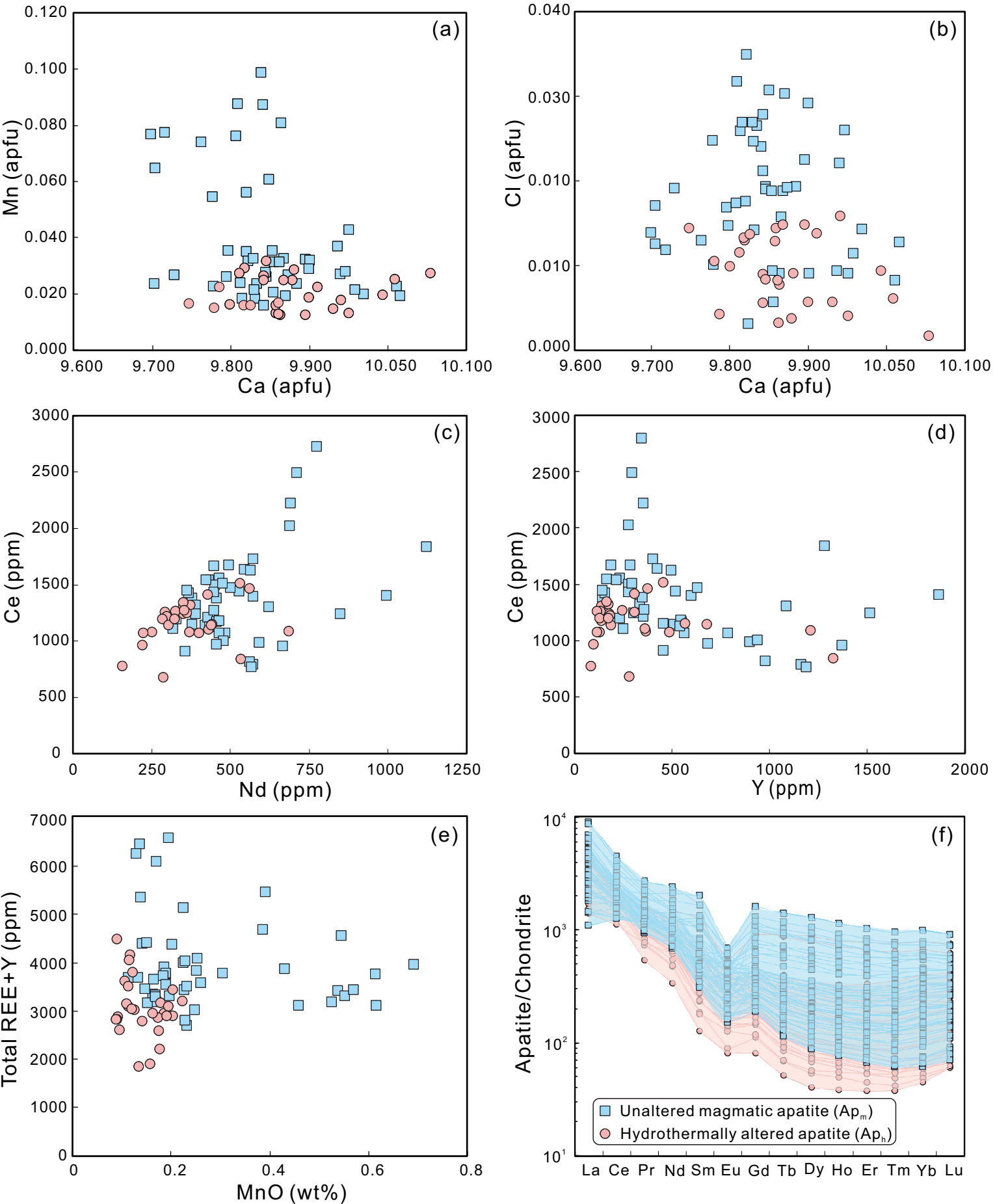
(a)
Mn (apfu)
Ca (apfu)
(b)
Cl (apfu)
Ca (apfu)
(c)
Ce (ppm)
Nd (ppm)
(d)
Ce (ppm)
Y (ppm)
(e)
Total REE+Y (ppm)
MnO (wt%)
(f)
Apatite/Chondrite
La Ce Pr Nd Sm Eu Gd Tb Dy Ho Er Tm Yb Lu
Unaltered magmatic apatite (Ap$_m$)
Hydrothermally altered apatite (Ap$_h$)

Figure 7

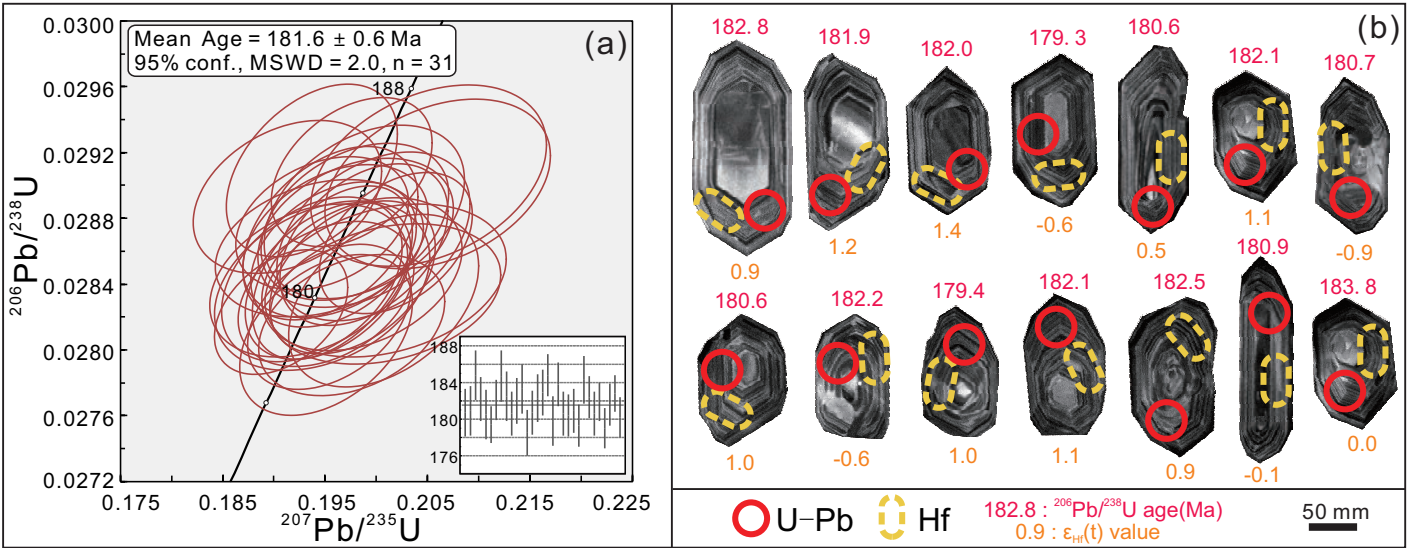
Mean Age = 181.6 ± 0.6 Ma
95% conf., MSWD = 2.0, n = 31
(a)
188
180
0.0300
0.0296
0.0292
0.0288
0.0284
0.0280
0.0276
0.0272
206Pb/238U
0.175
0.185
0.195
0.205
0.215
0.225
207Pb/235U
188
184
180
176
(b)
182. 8
181.9
182.0
179. 3
180.6
182.1
180.7
0.9
1.2
1.4
-0.6
0.5
1.1
-0.9
180.6
182.2
179.4
182.1
182.5
180.9
183. 8
1.0
-0.6
1.0
1.1
0.9
-0.1
0.0
U–Pb
Hf
182.8 : 206Pb/238U age(Ma)
0.9 : εHf(t) value
50 mm

Figure 8

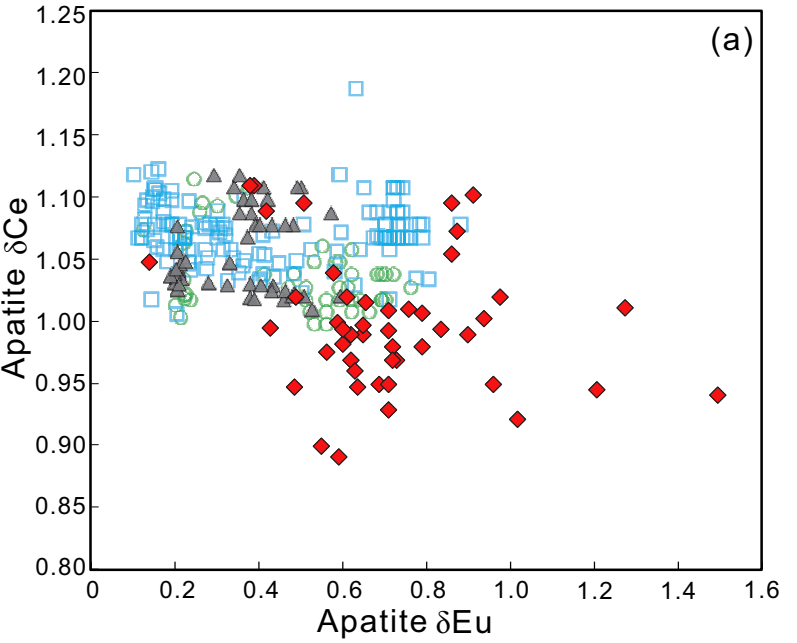
(a)
Apatite δCe
Apatite δEu
1.25
1.20
1.15
1.10
1.05
1.00
0.95
0.90
0.85
0.80
0
0.2
0.4
0.6
0.8
1.0
1.2
1.4
1.6

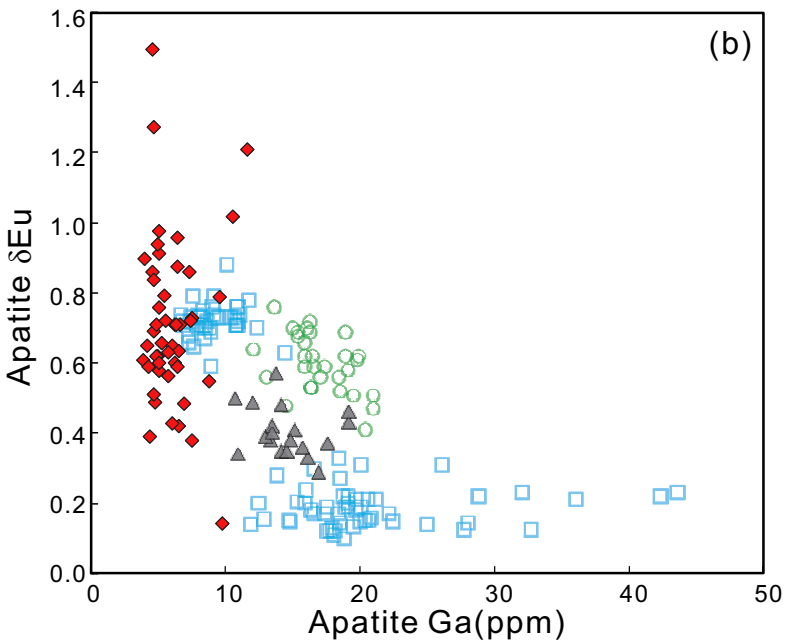
(b)
Apatite δEu
Apatite Ga(ppm)
1.6
1.4
1.2
1.0
0.8
0.6
0.4
0.2
0.0
0
10
20
30
40
50

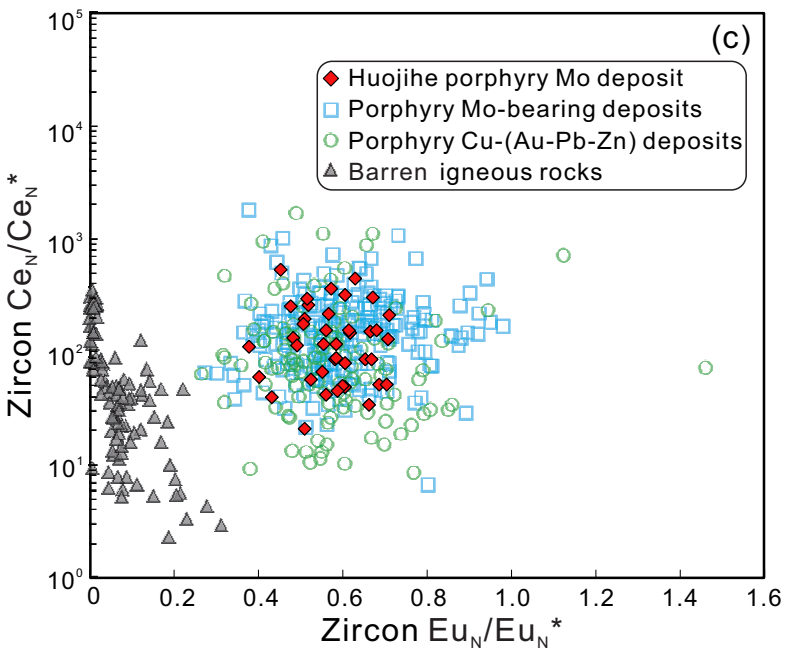
(c)
Huojihe porphyry Mo deposit
Porphyry Mo-bearing deposits
Porphyry Cu-(Au-Pb-Zn) deposits
Barren igneous rocks
Zircon Ce$_N$/Ce$_N$*
Zircon Eu$_N$/Eu$_N$*
10^5
10^4
10^3
10^2
10^1
10^0
0
0.2
0.4
0.6
0.8
1.0
1.2
1.4
1.6

Figure 9

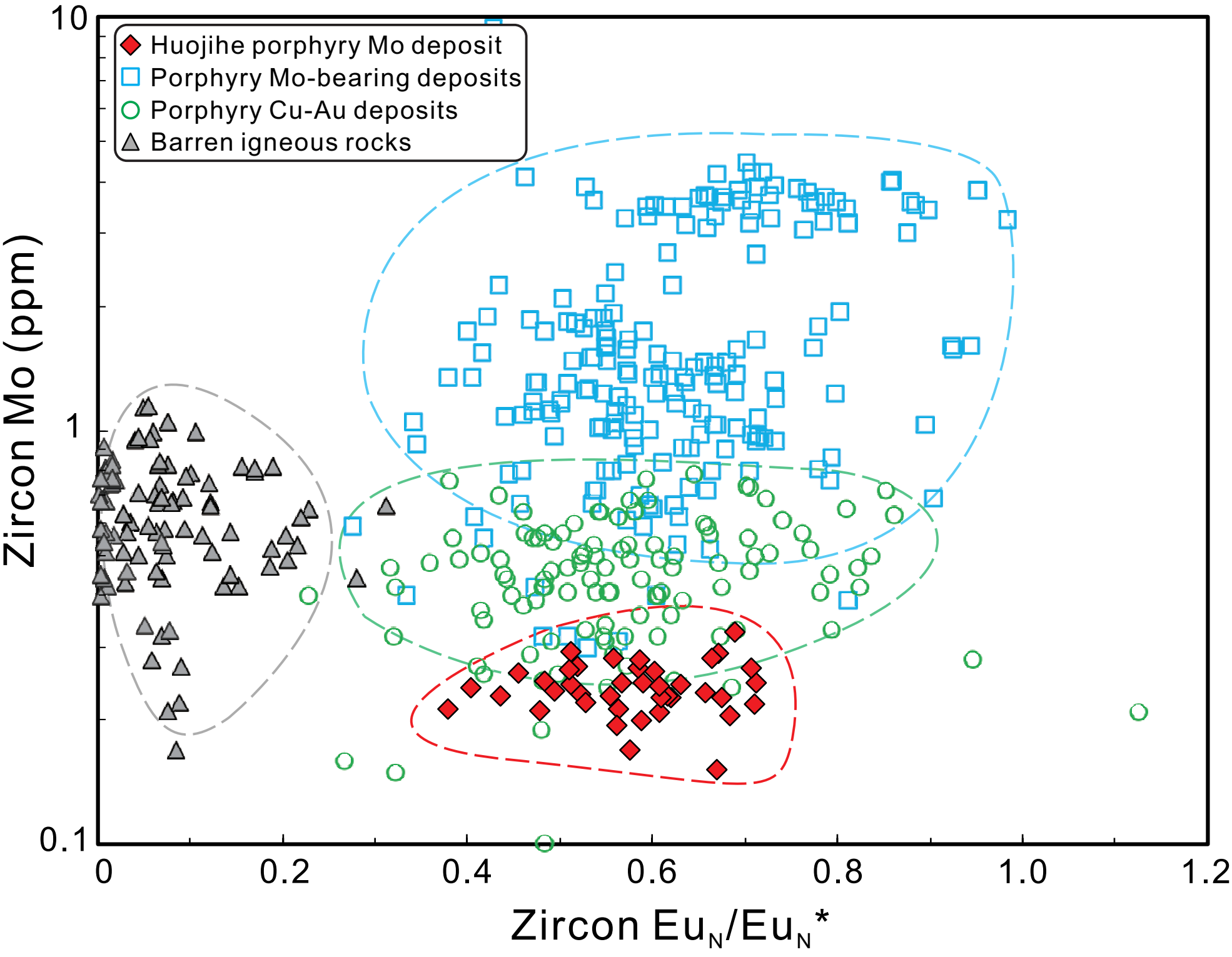
Huojihe porphyry Mo deposit
Porphyry Mo-bearing deposits
Porphyry Cu-Au deposits
Barren igneous rocks
Zircon Mo (ppm)
10
1
0.1
0
0.2
0.4
0.6
0.8
1.0
1.2
Zircon Eu$_N$/Eu$_N$*

Figure 10

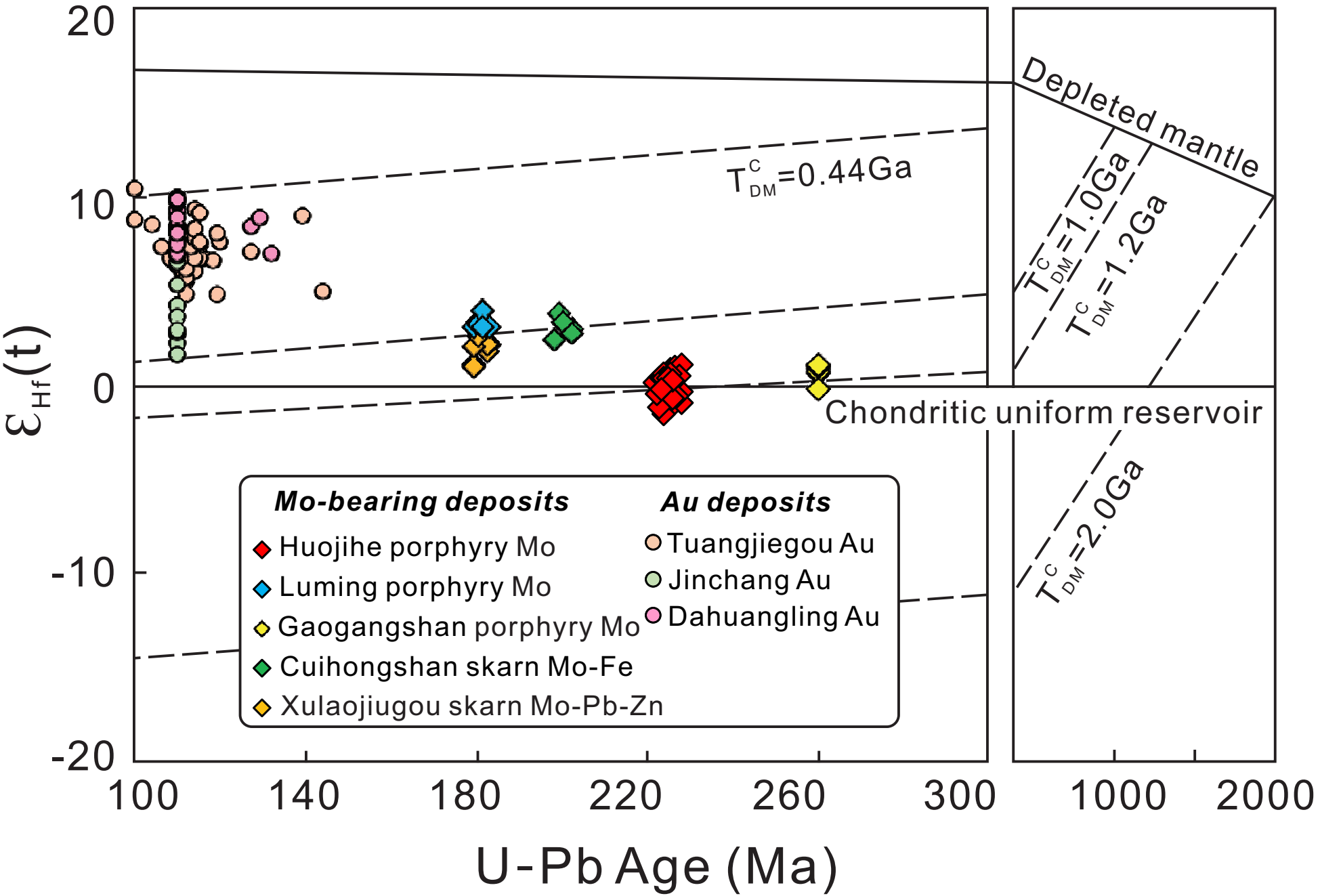
20
10
0
-10
-20
$\varepsilon_{Hf}(t)$
100
140
180
220
260
300
1000
2000
U-Pb Age (Ma)
Depleted mantle
T_{DM}^{C}=0.44Ga
T_{DM}^{C}=1.0Ga
T_{DM}^{C}=1.2Ga
T_{DM}^{C}=2.0Ga
Chondritic uniform reservoir
Mo-bearing deposits
Huojihe porphyry Mo
Luming porphyry Mo
Gaogangshan porphyry Mo
Cuihongshan skarn Mo-Fe
Xulaojiugou skarn Mo-Pb-Zn
Au deposits
Tuangjiegou Au
Jinchang Au
Dahuangling Au

Figure 11

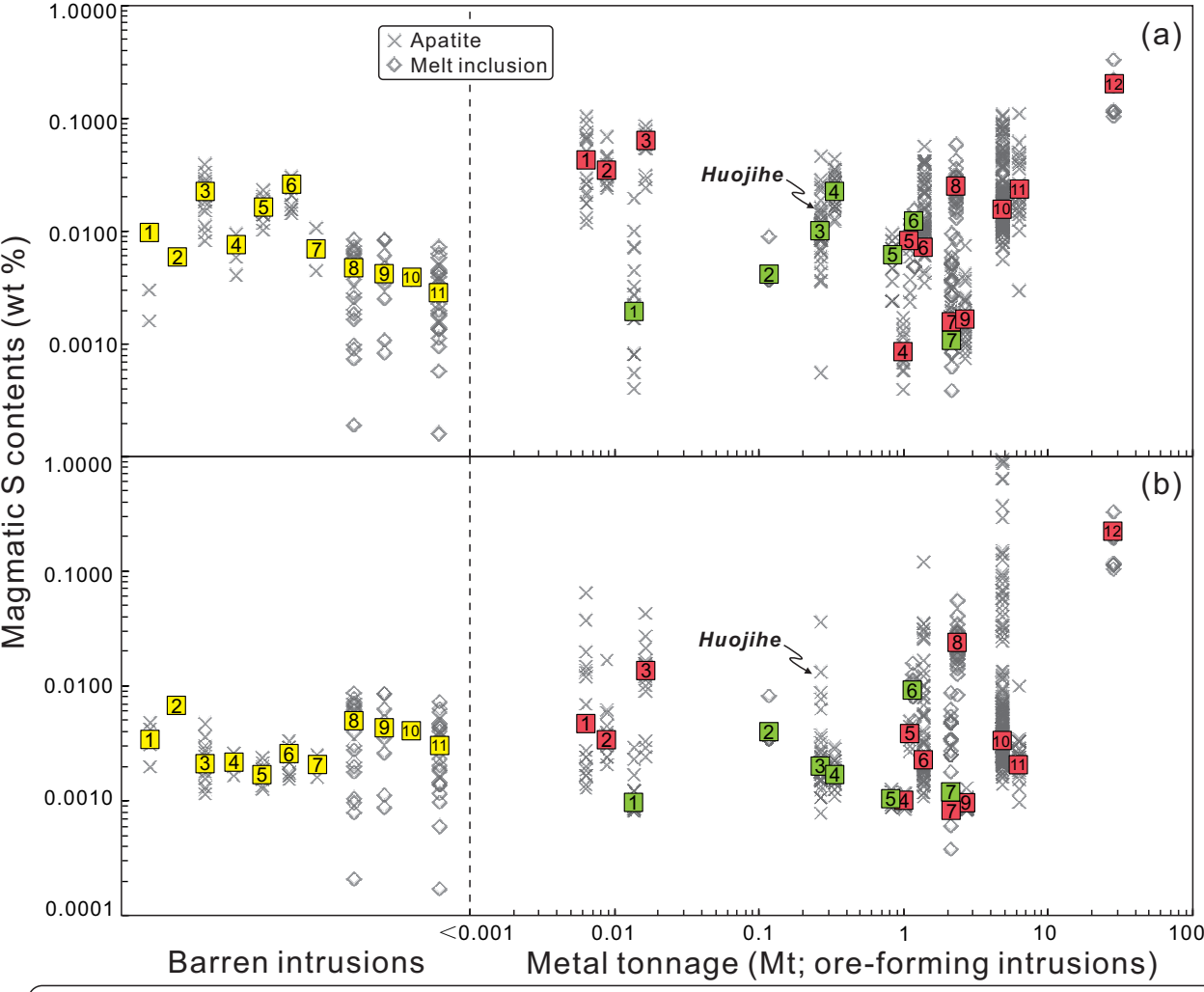

Barren igneous rocks: **1**-Clifton, **2**-Ligay (Binang), **3**-Bengqiaodi, **4**-Camp 6 (Black Mountain), **5**-Trassic Xiuwacu, **6**-Liujiawan, **7**-Bumolo (Waterhole), **8**-Late- to post-mineralization rhyolite porphyry dike of the Climax, **9**-Pre-mineralization white dike of the Alma district, **10**-Woods Mountain rhyolite of Henderson, **11**-Huangshan plutons

Porphyry Mo-bearing deposits: **1**-Xiuwacu, **2**-Silver Creek, **3**-Huojihe, **4**-Tongchanggou, **5**-Luming, **6**-Henderson,**7**-Climax

Porphyry Cu-(Au-Fe)/skarn/Fe-oxide Cu-Au deposits: **1**-Fuzishan, **2**-Niutoushan, **3**-Ouyangshan, **4**-Productora, **5**-Santo Tomas II, **6**-Carmen de Andacollo, **7**-Casualidad, **8**-Santa Rita, **9**-Candelaria, **10**-Coroccohuayco, **11**-Pulang, **12**-Bingham Canyon

Figure 12

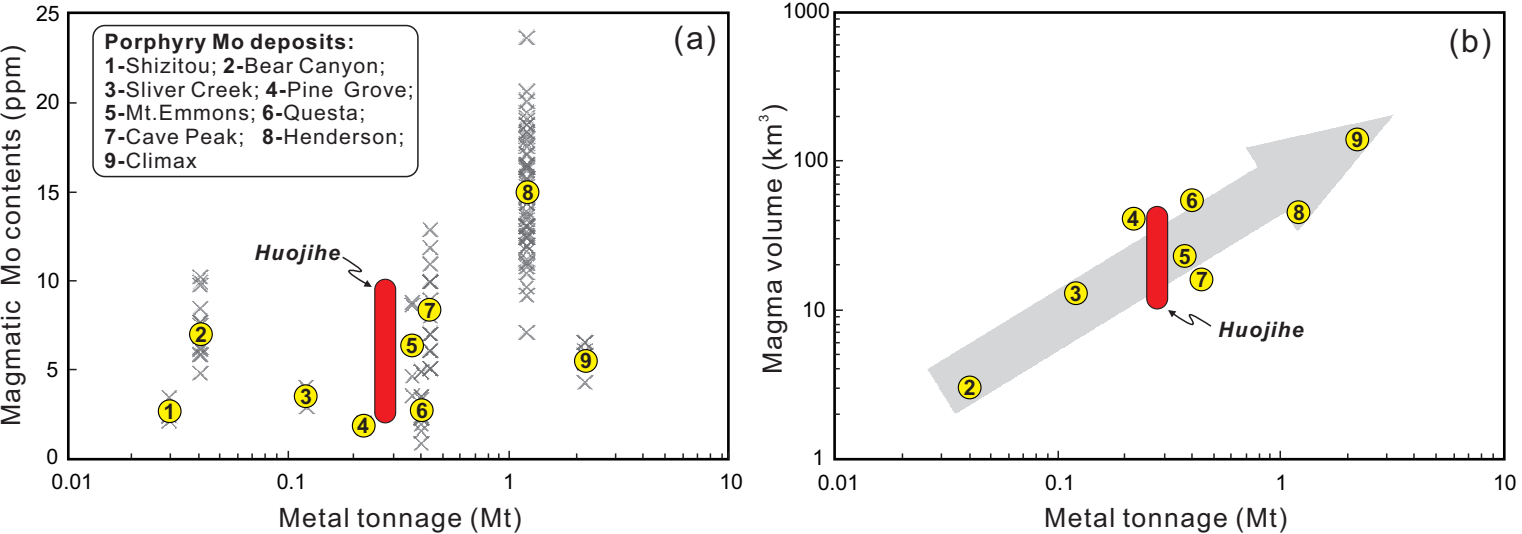
Porphyry Mo deposits:
1-Shizitou; 2-Bear Canyon;
3-Sliver Creek; 4-Pine Grove;
5-Mt.Emmons; 6-Questa;
7-Cave Peak; 8-Henderson;
9-Climax
(a)
Huojihe
Magmatic Mo contents (ppm)
Metal tonnage (Mt)
0
5
10
15
20
25
0.01
0.1
1
10
(b)
Huojihe
Magma volume (km3)
Metal tonnage (Mt)
1
10
100
1000